APPLICATION OF ATLAS 5 LARGE-AREA AND NANO-SCALE IMAGING TO PURPORTED VOLCANIC PRODUCTS OF THE EL LACO VOLCANO, CHILE

By

Joachim de Fourestier

A thesis submitted to the Faculty of Science
in partial fulfilment of the requirements
for the degree of
Bachelor of Science

Department of Earth Sciences
Carleton University
Ottawa, Ontario
April 2019

The undersigned recommend to the Faculty of Science acceptance of this thesis

APPLICATION OF ATLAS 5 LARGE-AREA AND NANO-SCALE IMAGING TO PURPORTED VOLCANIC PRODUCTS OF THE EL LACO VOLCANO, CHILE

submitted by **Joachim Ferdinand de Fourestier**

in partial fulfilment of the requirements of the degree of Bachelor of Science.

Dr. James E. Mungall, Thesis Supervisor
Department of Earth Sciences, Carleton University

Dr. Dirk Schumann, Thesis Co-supervisor
Fibics Incorporated

Dr. Robert F. Martin, Thesis Co-supervisor
Department of Earth and Planetary Sciences, McGill University

Dr. Dariush Motazedian, Chair
Department of Earth Sciences, Carleton University

Abstract

The El Laco iron deposit, located in the Chilean Andes, has more than 1.1 Gt (resources and reserves) of massive iron ore, dominantly in the form of magnetite. It formed in the late Cenozoic (Pliocene-Pleistocene) at shallow depths (<100 m) and relatively high temperatures, possibly above 1000°C. Texturally, the massive iron oxide rocks are vuggy and locally macrospherulitic and resemble extrusive rocks. However, this interpretation has been challenged, and some investigators suggest a purely hydrothermal mode of origin. The goal of this research is to shed light on the debate, by providing new observations in the form of a full suite of novel imaging datasets of El Laco ore samples. These include seamless correlation of large sample surfaces Zeiss ATLAS 5 imaging datasets (LM, FIB-SEM, EDS, 3D FIB-Nanotomography and 3D EBSD) from the macro- to nano-scale and tools to assist in the visualisation of quantitative information. Samples of unconsolidated tephra and of coherent lava have been examined using a novel workflow of optical and electron microscope images in a correlative workspace. Six different samples were analysed, looking at primary and secondary textures and phases. Using this workflow has enabled the discovery of what seemed to be simply well-formed oscillatory zoning to be micro- to nano-scale melt inclusions within magnetite grains from sample EL-JM-11. A target grain within this sample was then selected for closer examination by FIB-SEM to elucidate the composition and mineralogy of very small composite Ca-Mg-Si “droplets” suspected of being melt inclusions. This suite of techniques has allowed for the observation and interpretation of features that were previously inaccessible including micro-spherulitic iron oxyhydroxides and nano-sized melt inclusions. We hope this study along with the provided new data will help constrain whether the mineralizing fluid from which the iron ore was deposited was a hydrothermal fluid or a melt.

Acknowledgements

Firstly, I would like to express my appreciation for my supervisors Dirk Schumann, Robert “Bob” F. Martin and James “Jim” E. Mungall for their help on this thesis and for providing me the many interesting samples to my disposal. A thanks to Fernando Henriquez for his help and for providing lost information on some of the samples. A thanks to Fred Gaidies, as my second reader, for providing valuable input.

I would like to thank my father, Jeffrey de Fourestier, for inspiring me as child to become a geologist and for pushing me, when I needed it the most, to be the best I can be.

I would like to thank Mike Phaneuf for providing me with the opportunity of using this remarkable technology for my thesis and all the great people at Fibics for their support, friendship, and for providing an enjoyable working environment.

I would like to fellow thank Carleton University staff members Tim Mount (sample preparation technician) for his advice and help with the thin sections, and Maryam Shahabi Far (microbeam imaging and analysis specialist) for her help with EMPA analysis.

A thanks to the Society of Economic Geologists (SEG) Canada Foundation for funding part of this project.

A special thanks to Alex Koldewey, Gao Xiang “Geoffrey” Li, Marwan El-Ansassy and Thabiso Modise for their friendship and support. I would also like to give thanks to all my professors and fellow staff in the Department of Earth Sciences for their teachings, guidance and support during my time at Carleton University. And finally, a very special thanks to my parents and family friends for their unfailing support and continuous encouragement throughout my studies.

Table of contents

List of Tables

List of Figures

Introduction / Geological Background

The El Laco volcano complex (ELVC) is located within the Central Andes, Antofagasta region, Northern Chile. It has been dated at about 2.0 ± 0.3 Ma using K-Ar dating of andesite lavas and iron oxide ore (Naranjo et al., 2010) and has been described as a Kiruna-type deposit or rather an iron oxide-apatite (IOA) deposit (Dare et al., 2014; Hou et al., 2018; Nyström et al., 2016). It was described as a magmatic system with "magnetite lava flows" (Henriquez & Martin, 1978; Park, 1961; Travisany et al., 1995) based on field observations of its textures that show remarkable similarity to those of basaltic lava flows. The mineralization has been estimated to have more than 1.1 Gt (resource and reserves) of iron ore and remains one of the highest-grade deposits in Chile (CAP Mineria, 2017), occurring mostly as stratabound lenses (Tornos et al., 2016). The Laco Sur deposit alone has more than 0.5 Gt of ore, grading up to 60% Fe (Dare et al., 2015; Sillitoe & Burrows, 2002).

Somma volcano model (González Ferrán, 1974):

1. An andesitic stratovolcano is raised and possibly reaches 6000 m.a.s.l. over the rhyolitic plateau at approximately 4000 m.a.s.l.
2. As many other stratovolcanoes of the altiplano region (in South America's Central Andes) formed, it evolves and transforms into a caldera. Subsequently after a rhyodacitic eruption fractured the principal stratovolcano's structures, it collapsed and generated the El Laco Caldera. The last phase of this acid eruptive cycle consisted of a rhyodacitic central needle known as Pico Laco, which is cogenetic with the Pleistocene ignimbrite deposits (found below it).

3. A third andesite eruptive cycle starts with parasitic cones surrounding the Laco Caldera's Somma (an older caldera, generally a crater, that is partly refilled by a new central volcanic cone structure) ejecting andesitic lava flows.
4. A final fourth eruptive phase (likely the most recent from this volcanic complex) corresponds to the magnetitic flows extruded through the crater or the parasitic centers localized in the interior borders of the Caldera Laco's Somma (Laco Norte, Laco Sur, Rodados Negros, Tuyacho Alto) near 5200 m.a.s.l. In addition, a previous study (Thomas Novoa, 1970) has indicated the presence of itabirite (type of metamorphosed iron formation) partially digested inside the magnetite flows of El Laco as evidence for remobilization by the Pleistocene volcanic processes of sedimentary iron-rich rocks.

The host rock comprises andesite lava flows with rhyodacite intrusions (Henriquez & Martin, 1978; Mungall et al., 2018; Nyström et al., 2016). The El Laco debate rests on whether the origin of the magnetite mineralization is hydrothermal (Dare et al., 2015; Sillitoe & Burrows, 2002) or magmatic (Henriquez & Martin, 1978; Mungall et al., 2018; Nyström et al., 2016). Additional hypotheses have been proposed as a possible combination of the two (Knipping et al., 2015; Ovalle et al., 2018; Tornos et al., 2016). All over the world, the origin of Kiruna-type IOA deposits is still hotly debated, with the El Laco complex being one of the best-preserved examples (Dare et al., 2015; He et al., 2018).

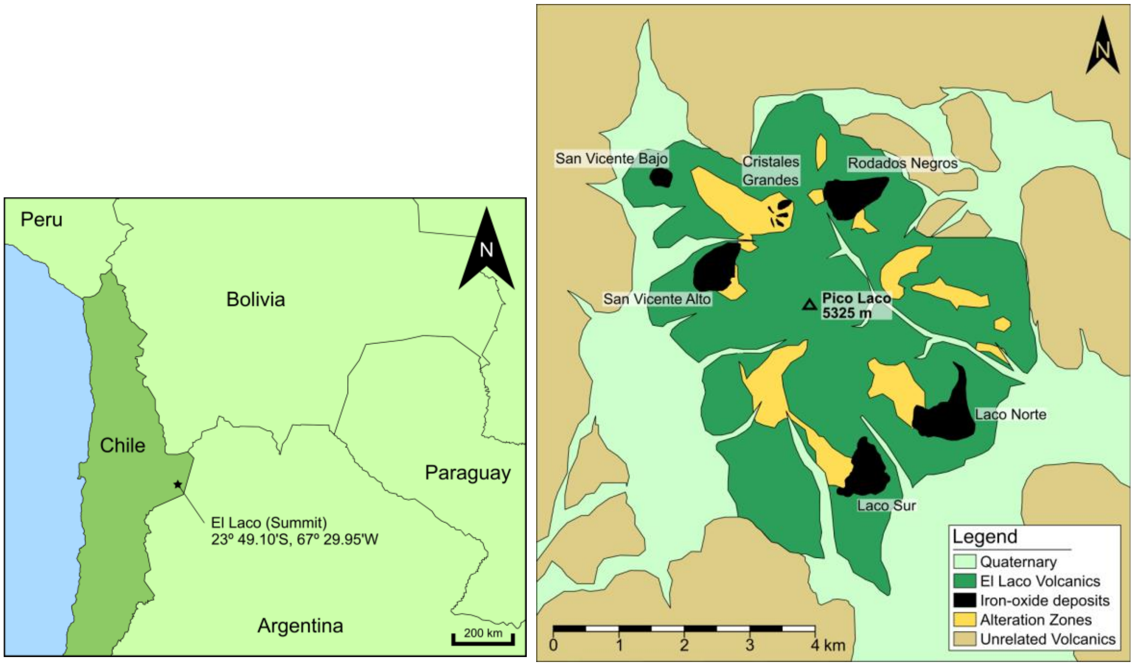

Figure 1 & 2: *(left) Location map of the El Laco volcano summit; (right) simplified geological map modified from Tornos et al., (2016) and Mungall et al., (2018).*

Determining the original primary phases and textures is difficult because of heavy hydrothermal overprinting (Dare et al., 2015; Henríquez & Nyström, 1998; Naranjo et al., 2010; Naslund et al., 2002; Sillitoe & Burrows, 2002). Previous authors have shown that the depth of formation of the magnetite mineralization could not have been greater than 300 m beneath the paleosurface: there is evidence of a steam-heated horizon in the vadose zone above the paleowater table (Sillitoe & Burrows, 2002). A more recent study has shown that mineralization is indicated to have been formed subaerially or at very shallow depth, no more than 100 metres below the surface; a considerable proportion of the unaltered andesite host preserved their original shapes (Tornos et al., 2016).

There are andesite, rhyodacite, intrusive and extrusive magnetite-rich bodies that are said to clearly post-date the ash-flow tuffs and ignimbrites of the Tertiary Altos de Pica formation (Henriquez & Martin, 1978) located 20° 30' S, 69° 11.8' E, but is more or less of similar age with other Plio-Pleistocene andesites in the area. Much of the iron oxide (primarily magnetite and hematite) is found as unconsolidated tephra (Mungall et al., 2018). Intrusive magnetite bodies show internal structures including dendritic or spherulitic crystal-growth forms that have been interpreted as veins or as feeder systems to overlying stratiform bodies. There is pervasive hydrothermal alteration thought be caused by volatile-rich fluids (Dare et al., 2015; Henriquez & Martin, 1978; Mungall et al., 2018; Nyström et al., 2016; Sillitoe & Burrows, 2002; Tornos et al., 2016).

Scapolite- and pyroxene-dominated alteration haloes have been found to be closely related to the massive magnetite. In addition, past fluid-inclusion studies conducted on the alteration minerals and vein fillings have shown that mineralization temperatures must have been high (710 – 840 °C or even higher) (Knipping et al., 2015; Sillitoe & Burrows, 2002). Pyroxene and apatite grains hosting microscopic fluid inclusions indicate that magnetite coexisted with anhydrite, an Fe-dominant (K-Na-Ca-Cl-SO_4) solid (> 80% vol.) within an aqueous vapor bubble coexisting with minor amounts of brine. Estimated temperatures range from 900 to 1300 °C, as indicated by oxygen isotope fractionation for these diopside-magnetite-anhydrite veins (Tornos et al., 2016).

At very high-temperature and very low-pressure conditions, phase diagrams show that saline aqueous fluid would predominantly be a vapour with little to no liquid water. A purely hydrothermal origin for the magnetite bodies appears unlikely due to the lack of liquid at such high temperatures, vapour being an inefficient transport for metal and the unlikely large amounts of fluids required to precipitate the 1.5 Gt of Fe oxide ore (Tornos et al., 2016). A purely magmatic origin is still debated owing to the unknown nature of Fe-P-O melts and whether or not these melts exist within the crust. Work with experimental Fe-C-P-O melts indicated that the magnetite and hematite deposits are very likely magmatic (Hou et al., 2018; Mungall et al., 2018). It has been proposed that an Fe-P-O liquid could have been erupted to the surface as ash and bombs (Mungall et al., 2018).

Another recent author has argued for a magmatic origin on the basis of observation of small well-preserved magnetite spherules found within pyroclastic material (Nyström et al., 2016).

The aim of this research is to shed light on the debate, by providing a full suite of high resolution large-area imaging datasets of El Laco ore samples and to investigate new features that were previously inaccessible.

Hand-sample descriptions

The following seven samples have been chosen to represent similar textures repeated over a wide range of length scales; a sample group with variety is more representative.

“Macrospherulite” sample (EL-BM-02)

This sample (see figure 3) is from Laco Sur where small magnetite spherules were found (Nyström et al., 2016), near the open pit of “friable ore”. The mineral assemblage in this fairly heavily altered sample is magnetite, apatite, hematite, possibly maghemite, and baryte, which occurs as relatively soft (< 5) white patches occupying small cavities within the iron oxides. The small cavities filled were only seen after sectioning to expose a less altered surface with small blob-like fillings, most of which are only a few millimetres in size, no larger than 1 cm in diameter. The hand sample’s approximate size is 17 x 16.5 x 10.5 cm. The sample has a dark-grey metallic lustre with significant portion of it being orange-brown likely from heavy hydrothermal alteration. There are many areas with foam-like vesicular textures that occur mostly on the outer edges of the radial or stellate growths of fine magnetite (and possibly apatite) needles ranging from 1 to 2.3 cm in length and no more than 1.5 mm in diameter (most of these are finer). These features, which are referred here as spherulites, appear to be floating in massive magnetite with their centres being slightly more vesicular than the rest of the sample, such as the relatively massive matrix.

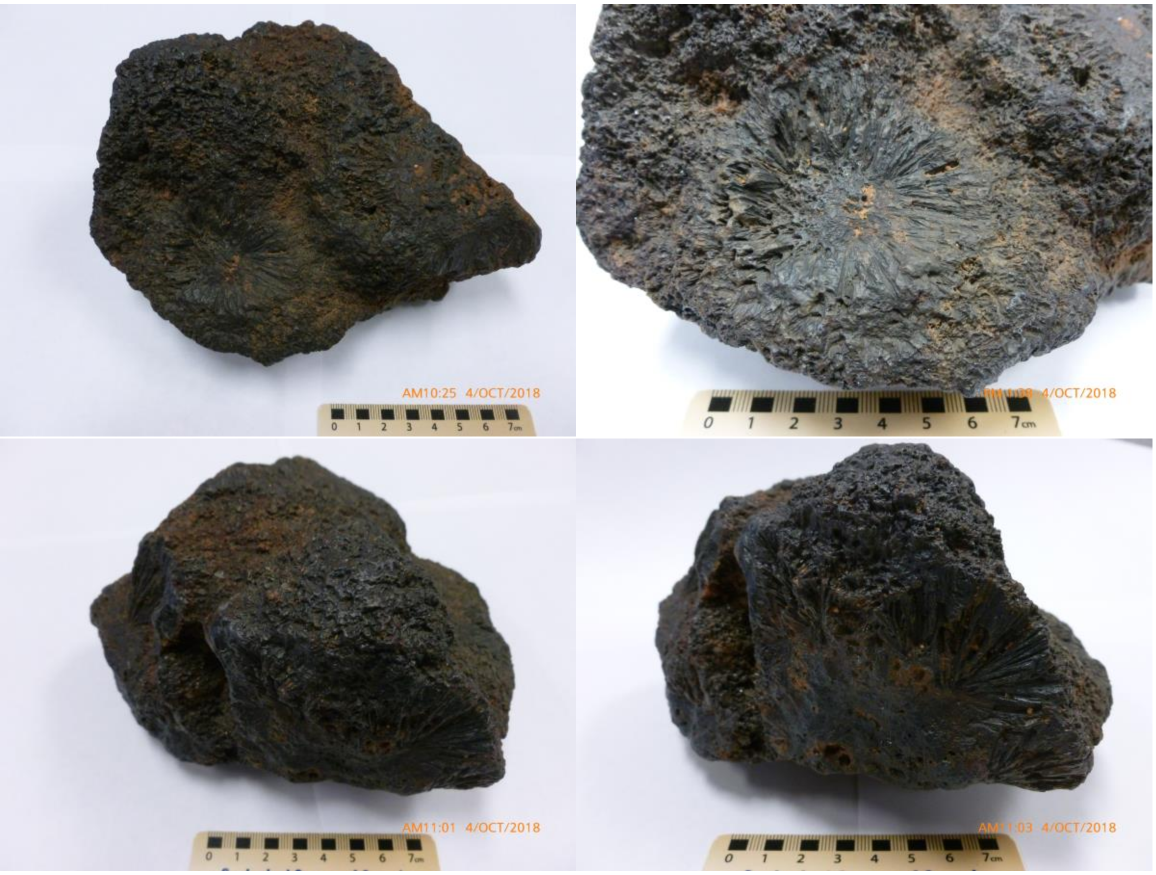

Figure 3: *Photos taken of the "macrospherulitic" magnetite sample EL-BM-02.*

Occasional small tubular holes are visible, leading from the outer edges of the spherulites towards the centre in between the needles. The "spherulites" range from 4 to 5.5 cm in diameter. There are many small holes throughout the sample, from 1 mm to 4 mm in diameter, possibly from weathering. Most of the pockets or vugs (which are sparse within this sample) are ~1 cm or less in diameter, but one is observed to be up to 5 cm in diameter with margins that are decorated by subhedral octahedra of magnetite 1 to 2 mm in size, suggesting growth into an open space occupied by vapour. There are some smaller "incomplete spherulites" or rather fans of magnetite needles. The whole sample is magnetic except for a few anomalous regions that repel a magnet or attract a small piece of iron. No particular distribution or pattern of these naturally magnetized domains was observed, and its significance remains unclear.

“Diktytaxitic” sample (EL-BM-03)

This hand sample (see figure 4) from San Vicente Bajo has an approximate size of 15.5 x 3.5 x 10 cm. This sample also has some distinct magnetized regions. The upper part comprises loosely amalgamated euhedral to subhedral dark octahedral magnetite crystals ranging from 3 to 7 mm in size, enclosing abundant pore space. If the porosity is considered to represent primary vesicles, then the resulting texture could be termed a coarse equivalent to diktytaxitic texture in crystal-rich silicate lavas (e.g., Mungall et al., 2018).

Figure 4: *Photos taken of the “diktytaxitic” magnetite sample EL-BM-03.*

Most of the sample is dark grey to brown-orange to even having certain spots of bright orange-yellow. There are many signs of alteration, such as soft ochrous material.

Numerous small cavities ranging from 0.5 to 2 mm in diameter may be solution pits. This sample also contains open pockets or vugs that are 0.6 cm to 5 cm in size lined with euhedral to subhedral 2 to 7 mm octahedral magnetite crystals. The lower part contains tubular voids within a matrix of massive magnetite. The tubes are oriented towards the top of the sample with all the magnetite octahedra.

"Columnar" sample (EL-BM-04)

This hand sample (see figure 5) was also collected in San Vicente Bajo and has an approximate size 8 x 4 x 6 cm. It is heavily altered, especially at the top that is almost completely bright orange-brown and weakly to not magnetic. However, the rest of the sample is magnetic with dark grey-brown to light brownish orange surfaces. The sample contains numerous individual magnetite columns whose terminations are subhedral to anhedral octahedrally shaped peaks (0.2 to 1 cm in diameter).

Figure 5: *Photos taken of the "columnar" magnetite sample EL-BM-04.*

On a sawed surface perpendicular to these individual columns, a distinct “columnar” breakage pattern is revealed, following a rough honeycomb-like pattern. These columns seem to represent many individual magnetite crystals that show an elongated growth with some hematite on the weathered surface. A fresh cut surface has a metallic dark-grey lustre, and in between the columns there are tubular voids extending from the bottom to the top of the sample where they are visible as small holes. The columns have a characteristic growth pattern of parallel to subparallel striations perpendicular to the elongation direction of each column. That said, the sample is frail owing to the abundant tubular holes.

Figure 6 & 7: *(left) Another photo of a “columnar” magnetite sample not used in this study, but with a more defined texture; (right) Sketch of the texture in question.*

Figure 6 shows another El Laco sample where the columnar texture is slightly better preserved and more visible. Columnar magnetite was previously observed and described as elongate or uniform prismatic arrays growths of magnetite dendrites (Henriquez & Martin, 1978; Nyström & Henriquez, 1994).

“Chilled contact margin” sample (EL-BM-01)

This sample, superficially resembling a chilled margin of comb-textured magnetite (“outer layer”) and apatite against friable fine-grained magnetite (“inner layer”), was collected in San Vicente Bajo, and has an approximate size of 13 x 7 x 5.5 cm. The weathered surface is grey-brown, whereas a fresh surface is dark grey, composed of mostly magnetite with lesser amounts of light grey-green apatite. The sample is highly magnetic. The outer layer is rather massive magnetite (individual grains not visible) containing abundant hexagonal euhedral to subhedral fractured apatite crystals ranging from 1 to 7 mm in diameter. The apatite crystals reach up to 2.3 cm in length occurring perpendicularly to the (sinuous) contact with the inner layer (see figure 8). All crystals of apatite within this outer later seem to be rooted from this division. The outer layer also contains many square cavities possibly due the dissolution of elongate crystals of a tetragonal or orthorhombic mineral, that are 1 to 3 mm in diameter and similarly positioned and distributed as the apatite crystals. The inner layer has a more equigranular appearance and is relatively rich in open pore space. There is a considerable number of ~1 mm diameter round cavities, possibly vesicles within the matrix of the inner layer.

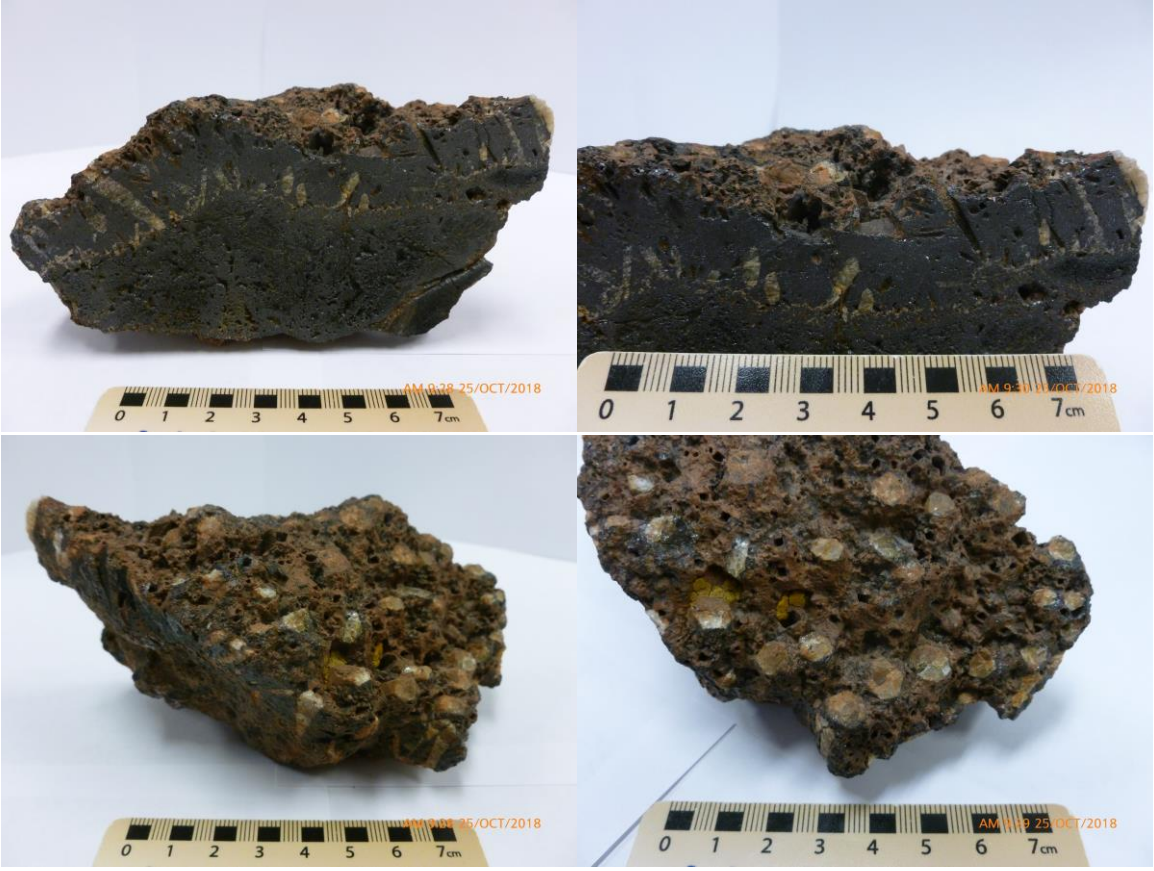

Figure 8: *Photos taken of the "chilled contact flow-like margin" sample EL-BM-01.*

Similarly to the outer layer, it has massive magnetite but seems to be composed of euhedral to subhedral octahedra no larger than 1 mm in size along with many included small apatite and possibly quartz crystals that are 1 to 2 mm in size. In additon, it has many small vesicles < 0.5 mm in size that are irregularly shaped, reaching lengths of up to 4 mm.

“Welded tuff” sample (EL-JM-11)

This magnetic hand sample was collected at Laco Sur, and was obtained from a previous study (Mungall et al., 2018) as sample EL-96-11. The sample contains very fine-grained (grains are < 0.2 mm in size) magnetite octahedra with poorly defined layers resembling a welded tuff with little to no visible signs of alteration or weathering. Between the magnetite crystals there is a well-connected diktytaxitic porosity throughout the sample.

Figure 9: *Photos taken of the magnetite “welded tuff” sample EL-JM-11.*

“Magnetite vein cutting Andesite” sample (EL-JM-82)

This hand sample, approximately 12.1 x 1.8 x 5.2 cm in size, accompanied with a thin section, was obtained from a previous study (Mungall et al., 2018) as sample EL-96-82. It is a slab cut of vesicular beige andesite with ochrous material filling in numerous solution cavities or primary vesicles, cut by a magnetite vein that is 3 to 6 cm wide and containing angular silicate (K-feldspar and quartz) rock fragments. Overall, the sample is significantly altered with darkened orange haloes around the cavities.

Figure 10: *Photo of a cut slab of an andesite bomb sample, EL-JM-82.*

"Unconsolidated tephra" sample (EL-JM-P4)

This sample is an epoxy mount of unconsolidated granular iron-oxide material from Laco Sur's "friable ore", possibly tephra, that was obtained from previous study (Mungall et al., 2018).

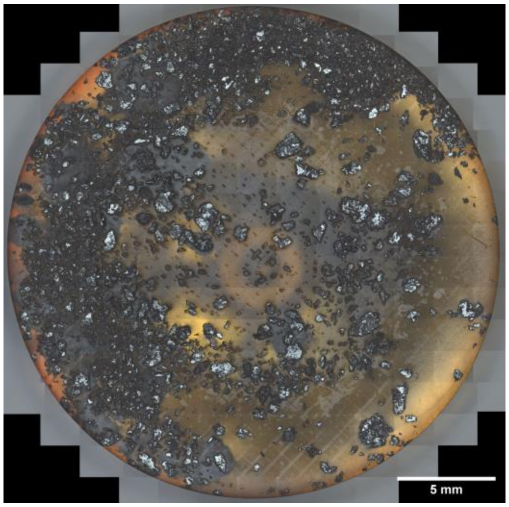

Figure 11: *Reflected light mosaic of the epoxy mount sample EL-JM-P4.*

This coarse powder consists of grains with a metallic lustre, most of which are 0.5 mm or smaller in size with a few exceptions that are no larger than 1 mm. These grains are primarily composed of hematite that occurs extensively throughout Laco Sur. A considerable proportion of the iron ore at El Laco is found in this form but has received little attention (Mungall et al., 2018). Similar hematite tephra samples at another locality contain unaltered pollen, suggesting that such material has not been affected by hot fluids (Corona-Esquivel et al., 2010).

Methodology

Thin-Section Preparation

Larger hand samples were trimmed using an 18-inch diamond blade rock saw (model 18-H, Serial No. Z563) manufactured by Great Western Equipment Co. (Chula Vista, California). Smaller hand samples were cut using a lapidary trim saw (model TS10) manufactured by LORTONE Inc. (Mukilteo, WA USA 98275). Pieces were trimmed off the samples and cut into slabs smaller than 27 x 46 mm with an approximate thickness of 1 cm. These were then sent to thin section labs for the preparation of polished petrographic thin-sections with a standard thickness of 30 µm.

Light Microscopy (LM)

Polarized light microscopy (PLM) was used for preliminary mineral identification and textural observations. This provided helpful reference images for subsequent scanning-electron microscopy imaging. Different minerals have distinct properties under polarized light. Since all the samples dominantly contain opaque minerals (mainly magnetite), reflected light (RL) was preferentially used over transmitted light (TL).

Using a Zeiss AXIO Zoom.V16 with AxioCam 506 Color, large-area reflected-light microscopy image mosaics were acquired and stitched with the software “ZEN Pro” version 2.5 using a coaxial reflected light source with the Plan Apo Z 0.5/0.125 objective (FWD 114 mm) at a resolution of 811 nm/pixel.

Samples for this study include six thin sections (EL-JM-11, -82; EL-BM-01, -02, -03, -04) and one grain mount of tephra (EL-JM-P4).

Carbon Coating

Carbon coating is performed to reduce charge build-up on the surface of samples when they are being analysed with an electron-beam instrument such as an SEM. Other types of coating such as gold, palladium or platinum can be used for superior prevention of charging. However, the high density of these elements can hinder on the quality of X-ray analysis methods such as EDS (Energy-Dispersive X-ray Spectroscopy) or WDS (Wavelength Dispersive X-ray Spectroscopy) commonly used in EPMA (Electron Probe Micro-Analysis) because of the extreme attenuation of emitted X-rays by the coating material.

Carbon coating was performed using a Leica EM ACE600 coater with the following parameters: minimum vacuum of 7.05×10^{-5} mbar, working distance of 70 mm, sample height of 2 mm, tilt of 0 degrees, method as “Double Pulse”, material as CT (carbon thread), thickness of 20.0 nm, for all thin-section samples. For the grain mount sample (EL-JM-P4), the only different parameter was a different working distance in order to account for the larger sample height of 15 mm.

Scanning Electron Microscope (SEM) Imaging

To obtain magnified images and other useful information beyond the level of optical microscopy, the scanning electron microscope (SEM) is a common instrument of choice owing to its versatility and adaptability; it can be used to obtain morphologic, topographic, crystallographic, compositional and other various chemical and physical information. The instrument uses a high-energy focused electron beam that is directed down a column with a series of accelerating magnetic lenses towards a sample within a vibration-free vacuum chamber. This electron beam can be produced either thermionically (e.g. using a tungsten filament) or using field emission guns. The SEM has overlap with other instruments such as an electron probe micro-analyser (EMPA) but the basic principle remains the same other than various added apparatus or detectors to enable other capabilities. As the electron beam interacts with the sample, many different signals can be detected and measured, primarily backscattered electrons (BSE) and secondary electrons (SE); BSE response shows chemical differences by contrast: it is typically brighter for heavier elements, whereas SE response is typically brighter for topographically higher surfaces (Goldstein et al., 2017) .

ATLAS 5 Large-Area Imaging

ATLAS 5 is a combined system of hardware and software that allows for efficient sample navigation of correlated data from various sources (such as LM, SEM, FIB-SEM, EDS, etc.). Large-area mosaics are scanned or rather imaged as the system simultaneously acquires images tile by tile from multiple signals (see figure 13). Other sources maybe imported later on within the correlative workspace where each source and various capture regions are aligned and appear as layers. What is obtained is a stacked set of images in which each layer can be leveled with transparency and all levels are navigated synchronously. ATLAS 5 allows one to quickly scan and identify different features, better assuring one of not missing tiny features that could have been missed otherwise.

The SEMs used for the study are the Zeiss EVO MA 15 tungsten filament SEM and Zeiss GeminiSEM 450 field emission SEM, both located at Fibics Incorporated (Ottawa, Canada). The large-area light microscopy mosaics obtained beforehand (with the Zeiss AXIO Zoom) are imported and re-stitched in ATLAS 5, then aligned with the sample in the SEM to begin acquiring large-area SEM image mosaics using the imaging parameters show in Table 1a. After the mosaics are acquired, aligned, image-corrected and stitched, these are then exported to a series of autonomous files as the ATLAS Browser-Based Viewer (BBV) web application. This enables anyone on a computer with a web browser to explore and navigate the sample interactively in a similar fashion to the well-known

"Google Maps™" web mapping application. In order to facilitate the workflow, new features and other improvements were implemented as it was being used during this study.

Table 1a: SEM imaging conditions and parameters

	EL-JM-11	EL-JM-82	EL-JM-P4	EL-BM-01	EL-BM-02	EL-BM-03
Machine (SEM)	GeminiSEM 450-70-63	GeminiSEM 450-70-63	GeminiSEM 450-70-63	EVO 15-14-71	GeminiSEM 450-70-63	EVO 15-14-71
EHT (kV)	15.0	15.0	15.0	20.0	15	20.0
WD (mm)	11.735	10.174	9.779	11.695	11.003	10.579
Beam current (nA)	3.1	3.1	1.4	2.2	1.4	2.3
Detector	BSE	BSE	BSE & SE	BSE	BSE	BSE & VPSE
Dwell time (µs)	4.000	4.000	4.000	3.000	4.000	3.000
Resolution (nm/pixel)	149.7	139.2	149.8	163.2	149.9	200.0
Tile size (pixels)	4096 x 4096	4096 x 4096	5120 x 5120	4096 x 4096	5120 x 5120	3072 x 3072
Tile size (FOV) (µm)	614.3 x 614.3	572.4 x 572.4	766.9 x 766.9	655.5 x 655.5	766.9 x 766.9	614.3 x 614.3
Mosaic tiles	1949	2237	962	2757	1799	2579
Pixel count (gigapixels)	32.7	37.5	25.2	46.3	47.2	24.3

Acronyms used: BSE: back-scattered electron, EHT: electron high tension, FOV: field of view, SE: secondary electron, VPSE: variable pressure secondary electron, WD: working distance.

BBV Exports (available for viewing online):

- **San Vicente Bajo**
    - http://petapixelproject.com/mosaics/joedf/El-Laco/EL-BM-03
    - http://petapixelproject.com/mosaics/joedf/El-Laco/EL-BM-04
- **Laco Sur**
    - http://petapixelproject.com/mosaics/joedf/El-Laco/EL-BM-01
    - http://petapixelproject.com/mosaics/joedf/El-Laco/EL-BM-02
    - http://petapixelproject.com/mosaics/joedf/El-Laco/EL-JM-11
    - http://petapixelproject.com/mosaics/joedf/El-Laco/EL-JM-82
    - http://petapixelproject.com/mosaics/joedf/El-Laco/EL-JM-P4

Energy-dispersive X-ray Spectroscopy (EDS/EDX)

Amongst other signals produced when the beam interacts with the sample, distinct X-rays can be measured to obtain compositional information. When the incident energy of the beam exceeds the critical ionization energy of an element, a specific characteristic X-ray is emitted representative of that atomic shell (Goldstein et al., 2017).

In contrast to EMPAs which primarily use wavelength-dispersive spectroscopy (WDS) for elemental composition, EDS has shorter acquisition times, making it very useful when quickly surveying a sample. Since WDS has much higher precision, EDS is generally used qualitatively prior to acquiring quantitative values with the former. It works well for major elements, whereas WDS permits both major and trace element analysis. That said, quantitative analysis can be performed when using a standard and the relative intensities of the constituents: the instrument can be calibrated to an element with known values (Goldstein et al., 2017; Newbury & Ritchie, 2013).

The EDS system is generally accompanied by analytical software to help identify the characteristic X-ray peaks in the spectrum of specific elements. In addition, the software may calculate quantitative values with complex matrix correction once the device is calibrated to a standard. However, some spectra will have interferences with others: differentiation and interpretation of overlapping peaks require experience (Goldstein et al., 2017). So-called “forbidden elements” such as REE, conflict with many elements (Newbury & Ritchie, 2013).

Table 1b: EDS analysis conditions and parameters

Machine (SEM)	ZEISS EVO MA 15-14-71
EHT (kV)	20.0
WD (mm)	~ 10.4
Probe current (nA)	~ 2.3
Detector	2 x Bruker XFlash 6|30
System and Software	Bruker Quantax 200, ESPRIT v1.9

Acronyms used: EHT: electron high tension, WD: working distance.

The EDS element maps in this study were produced using Bruker’s Quantax 200 system set up on the Zeiss EVO MA 15 equipped with two Bruker XFlash 6|30 EDS detectors. These element maps are a bitmap representation of the element concentrations where the pixel colour represents a specific element and the brightness or intensity of the pixel is its relative concentration. The EDS analyses were performed using the software and operating conditions shown in Table 1b. However, these all vary a little when changing magnification and focus. The acquired element maps and point analyses were exported from the software, combined, and image-edited into figure plates. Subsequently, these EDS figure plates were linked with the region of acquisition in the respective BBV exports of each sample.

Electron Microprobe Analyser (EMPA / EPMA)

Quantitative analyses were carried out with an automated four-spectrometer Cameca Camebax MBX electron microprobe by wavelength dispersive x-ray analysis method (WDX) at the Earth Sciences department, Carleton University, Ottawa. Background positions were carefully selected to avoid instances of peak overlap. Background measurements were made at 50% peak counting time on each side of the analysed peaks. Raw x-ray data were converted to elemental weight % by the Cameca PAP matrix correction program. A suite of well-characterized natural and synthetic minerals and compounds were used as calibration standards (see tables 2, 3 and 4). Calibration was tested by analysing known compositions (mineral standards) as unknowns (Evan Garnet and for silicates and oxides, BRGM apatite for phosphates, REE glass for REE minerals, see Appendix).

Operating conditions

The following parameters were used: 15 kV accelerating voltage, 23 nA beam current for apatite and Fe phosphate, and 20 kV accelerating voltage, 22 nA beam current for other minerals. A focused electron beam was used for oxides and defocused (rastered, ca. 8µm in diameter) electron beam for other minerals. The counting times for S, P, F, Cl and REE (rare-earth element) were 30 seconds and for other elements were 15-20 seconds, or 40,000 accumulated counts for all elements, whichever came first.

Table 2: EMPA standards for silicates and oxides

Element	Line	Standard
Si	Kα	synthetic Mg_2SiO_4
Ti	Kα	synthetic $MnTiO_3$
Al	Kα	synthetic $MgAl_2O_4$
Fe	Kα	synthetic Fe_2SiO_4
Mn	Kα	synthetic $MnTiO_3$
Mg	Kα	synthetic Mg_2SiO_4
Ca	Kα	wollastonite
Na	Kα	albite
K	Kα	microcline
S	Kα	baryte $BaSO_4$
P	Kα	synthetic $NaBePO_4$

Table 3: EMPA standards for apatite and iron phosphates

Element	Line	Standard
Si	Kα	synthetic Mg_2SiO_4
Fe	Kα	synthetic Fe_2SiO_4
Ca	Kα	BRGM apatite
Na	Kα	synthetic $NaBePO_4$
S	Kα	baryte
P	Kα	BRGM apatite
Cl	Kα	$Na_4AlBeSi_4O_{12}Cl$
F	Kα	BRGM apatite

Table 4: EMPA standards for sulphates

Element	Line	Standard
Fe	Kα	synthetic Fe_2SiO_4
Ca	Kα	wollastonite
S	Kα	baryte $BaSO_4$
Sr	Lα	synthetic $SrTiO_3$
Ba	Lα	baryte $BaSO_4$

Focused Ion-Beam (FIB) and 3D FIB-Nanotomography

A FIB-SEM is a generally a “dual beam” machine (see figure 12), having an electron beam for imaging (SEM) and an ion beam (FIB) for milling and sputtering (Goldstein et al., 2017). Although inert gases such neon, argon and xenon can be used as an ion source, the ion beam more commonly uses a liquid metal ion source (LIMS). Conventionally, gallium is most used, primarily because of its low melting temperature (~ 29.8 Celsius) and low volatility at the melting point amongst numerous other reasons (Goldstein et al., 2017). A reservoir of this LIMS is attached to a tungsten needle, permitting the liquid to trickle down to the needle tip, which has a diameter of about ~5 nm. The heated gallium wets the tip of the needle where an electric field is applied; this effectively ionizes the gallium ions by field evaporation. As ions of gallium leave the tungsten needle, they are continuously replaced as the liquid metal flows down and clings at the tip due to electrostatic forces (Giannuzzi & Stevie, 2005). The ions are accelerated down the column through a series of magnetic lenses (Goldstein et al., 2017) and apertures. The accelerating voltages range from 5 to 50 keV but are typically between 25 to 50 keV. Once the ion beam hits the sample (at a typical working distance of 2 cm or less) many different species/signals are produced ranging from secondary electrons to sputtered material (atoms, molecules) and secondary ions (Giannuzzi & Stevie, 2005). The key advantage is precision *in situ* modification of the sample by milling or sputtering, allowing for nano-scale cross-sectioning and imaging (Goldstein et al., 2017).

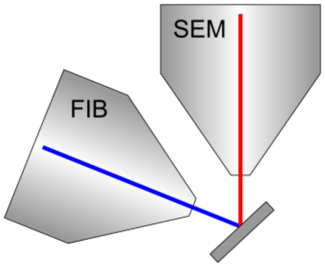

Figure 12: *A schematic drawing of the FIB-SEM "dual beam" machine.*

The energy selective backscattered (EsB) Detector[1] is used instead of the conventional BSE detector, because there are technical limitations of the detector such as having physically overlapping positions within the instrument chamber with respect to the sample. EsB captures electron signals direct up the column instead of at an angle like BSE.

Two to four different streams of data are collected simultaneously during FIB-nanotomographic imaging: a FIB mills (sequentially slicing away cross-section thickness within the order of a few nanometres) while an electron-beam (EsB and BSE) images at a different angle. After the removal of every 10 or so slices, EDS and or EBSD (see below) imaging is performed. This is not done at every slice because of time efficiency (stage positioning and rotation, conditions different) and effective data for the level of coarseness.

---

[1] For more information, see https://www.zeiss.com/content/dam/Microscopy/Products/electron-microscopes/upgradesEM/pdf/upgradeinfo-esb-detector.pdf

Then, all slices are stacked and extruded with an appropriate thickness to create a 3D reconstruction model of the sample volume that was milled away. This model can then be segmented based on a property such as a certain threshold of signal intensity to observe particular grains or materials of interest.

A 3D FIB-nanotomography run was conducted on a ZEISS Crossbeam 550 L with ATLAS 3D on a selected in sample EL-JM-11 (see figure 46). This resulted in 5135 slices (see figure 47) with a pixel size of 5 nm, tile size of 8128 x 8128 pixels, using a dwell time of 0.3 μs and an EHT of 2.0 kV at 2.1 nA, capturing with EsB and SESI (secondary electron or secondary ion)[2] detectors simultaneously. However, the run was cut short at around 3591 slices owing to technical difficulties: the ATLAS 3D run started at 23/01/2019 15:06:54 and ended at 28/01/2019 07:11:37 giving a total duration of 4 days, 16 hours, 4 minutes and 43 seconds. Slice 3591 was imaged at: 27/01/2019 02:32:26, meaning the kept slices took total of 3 days, 11 hours, 25 minutes and 32 seconds to complete.

3D Electron backscatter diffraction (EBSD)

To distinguish different grains of a single mineral phase, a sample can be steeply tilted (60° - 90°, but typically 70°), to change the angle of incidence of the electron beam with respect to the sample’s flat (very finely polished) surface. This increase in angle can increase or decrease the penetration depth of the beam depending on each individual grain’s crystallographic orientation and other properties. This effectively produces a weak but resolvable contrast in backscattered electron images. An extremely flat and fine polished surface is needed because the contrasting effects are typically obtained from

---

[2] For more information: https://www.zeiss.ca/content/dam/Microscopy/Products/electron-microscopes/upgradesEM/pdf/upgradeinfo-sesi-detector.pdf

within the first 10 to 100 nm depth of the sample's shallow near-surface layer (Goldstein et al., 2017).

To achieve such a surface, an additional final polishing stage must be performed. However, this must not be prolonged, as it could cause an excess in relief. Methods to achieve this include chemo-mechanical polishing, vibratory polishing[3] and ion beam polishing[4]. Normal abrasive polishing processes might otherwise deform the outmost 100 nm and subsequently obscure crystallographic orientation during analysis (Leica Microsystems, 2014; Oxford Instruments, 2018).

Taking advantage of the diffraction of backscattered high voltage electrons as well as the modulation of their backscatter intensities at different angles, electron backscatter diffraction (EBSD) patterns are produced. The diffraction patterns, also known as "kikuchi" lines, reveal symmetry, orientation and other important crystallographic information. Each of these lines or bands is parallel to a specific crystal plane, respecting the Bragg condition; angles between these and how these are organized with respect to each other can be used to calculate the space group and orientation.

The Bragg diffraction relation is given as,

$$n\lambda = 2d \sin \theta_B$$

where: n (integer) is the order of diffraction, λ is the wavelength, d is the spacing between atomic planes, and θ_B is the angle of incidence which critically changes the degree of electron channeling depending on a particular set of crystal planes (Goldstein et al., 2017).

---

[3] For more detailed information, see http://www.ebsd.com/hints-tips-for-ebsd-data-collection/ebsd-sample-preparation/polishing

[4] For more information, see https://www.leica-microsystems.com/science-lab/ion-beam-polishing-of-sample-surfaces-sample-preparation-for-sem/

As the FIB crosscuts the sample, the slices are measured for thickness and for EBSD patterns to essentially produce a 3D reconstruction of each grain, generally with different colours to differentiate crystallographic orientation (using a colour key or gradient diagram chart similarly to Michel-Lévy but for orientation).

EBSD combined with EDS for progressive indexing, and building a database of the patterns over time, can become a very powerful tool to identifying different phases with similar composition such as different types of steel, different polymorphs of specific chemical composition. In other words, this is achieved by combining chemical and crystallographic information.

In order to achieve this, the ATLAS 3D software was used to capture the 3D FIB-nanotomography dataset (see sample EL-JM-11 in results for the operating conditions).

Results

Sample EL-BM-02

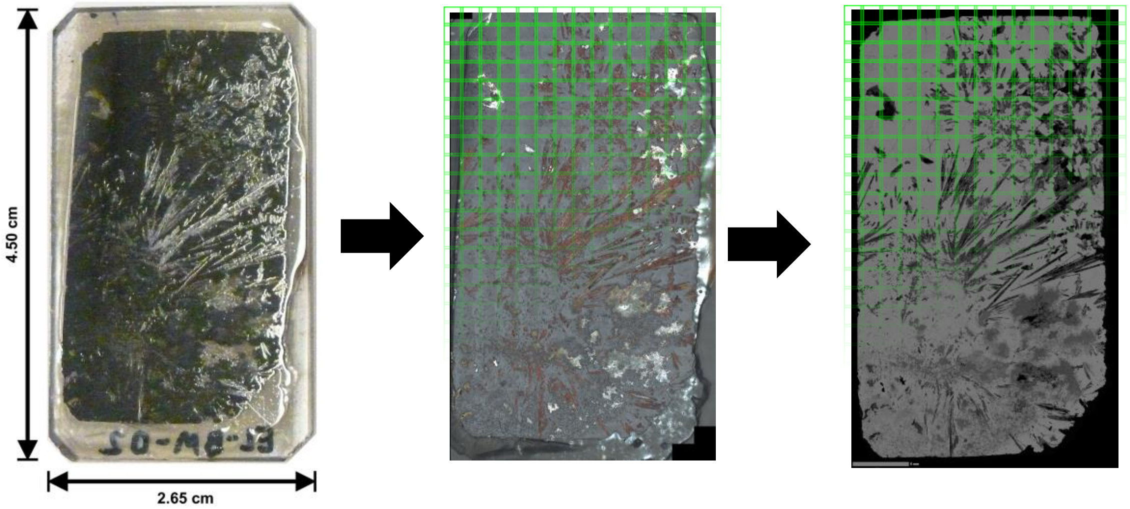

Figure 13: *A simplified diagram depicting the imaging process of the samples.*

A thin section (see figure 13) was prepared with a focus on the stellate, possibly rapid-growth textures. The section was cut-off from a smaller but representative spherulite in order to preserve the larger well-exposed spherulite. This sample preserves traces of the primary mineral assemblage, which permits one to infer the original textural arrangement. It also has a fairly complete paragenetic record of several superimposed alteration episodes.

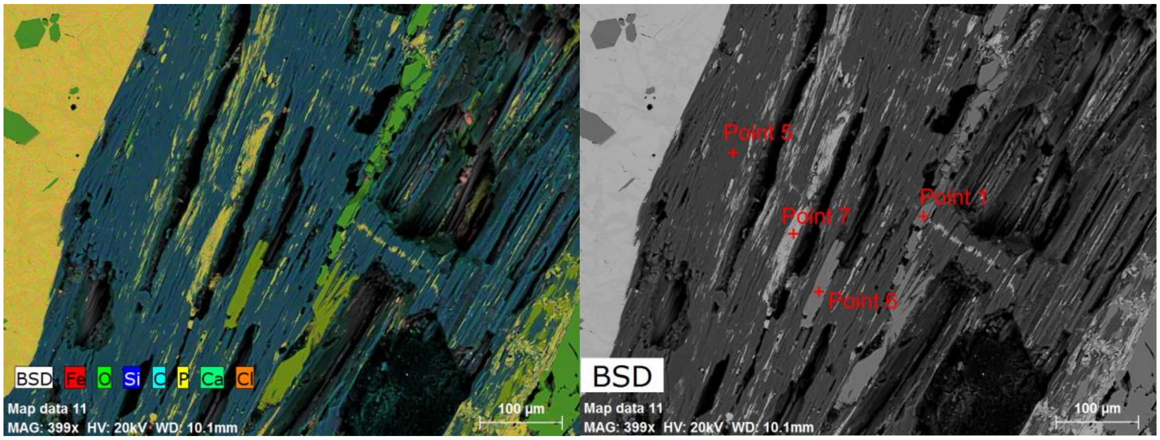

Figure 14: *EDS composite map 11 and BSE image of the stellate needles in EL-BM-02.*

Under PPL and XPL, the needles seem to dominantly be fluorapatite. The produced ATLAS 5 multi-resolution large-area SEM image mosaic of the thin section and the EDS chemical maps (see figure 14) have revealed the composition of the stellate needles to be much more complex (EDS point data is available in the appendix). Point 5 is almost pure silica (or rather a silicate originally). Point 6 shows strong signals for Fe-P-O, an unidentified iron phosphate phase. Point 7 is primarily Fe oxide with minor amounts of Si and P, most likely magnetite and hematite. Point 1 has strong signals of Ca, Si, P and O, possibly altered diopside or apatite. However, there are no signs of primary diopside observed within this sample. The stellate assemblage has a rather complex history. There are also cracks that are perpendicular to sub-perpendicular to the elongation of the needles, with the same backscatter signal as the magnetite matrix, possibly an altered Fe-O phase. These cracks crosscut the "apatite" needles, which in turn crosscut the zoning found in the magnetite matrix. Some of the zoned cracks found within the matrix connect with the perpendicular alteration cracks that crosscut the large apatite needles.

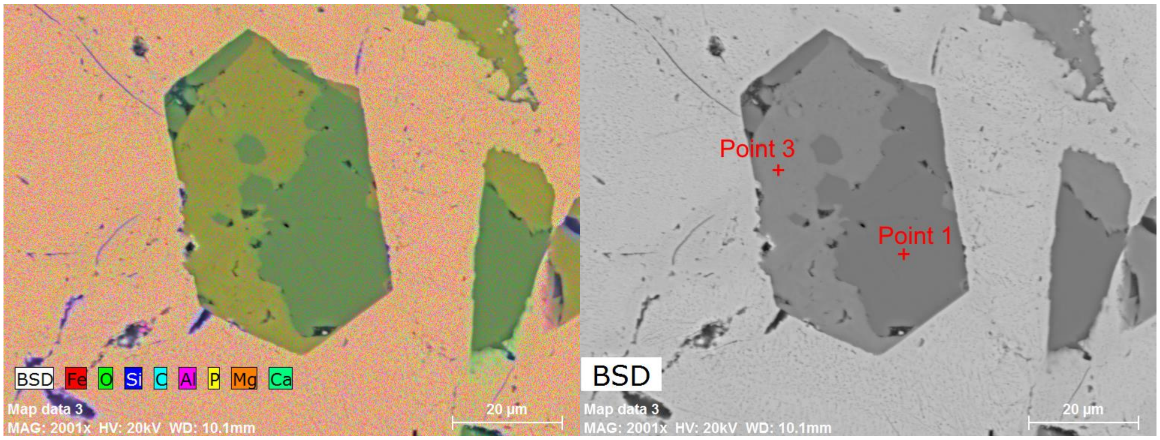

Figure 15: *EDS composite map 3 and BSE image of altered apatite crystals in EL-BM-02.*

In figure 15, the BSE image as well as the EDS composite map show a single euhedral grain of apatite, of about 60 µm across that has been partly altered to an unidentified (point 3) Fe-P-O pseudomorph phase. Point 1 was analysed under EMPA to be fluorapatite (see appendix for EDS and EMPA point data). This type of Fe alteration can be observed throughout the sample such as other apatite grains, or filled cracks changing in composition from apatite to Fe-P-O.

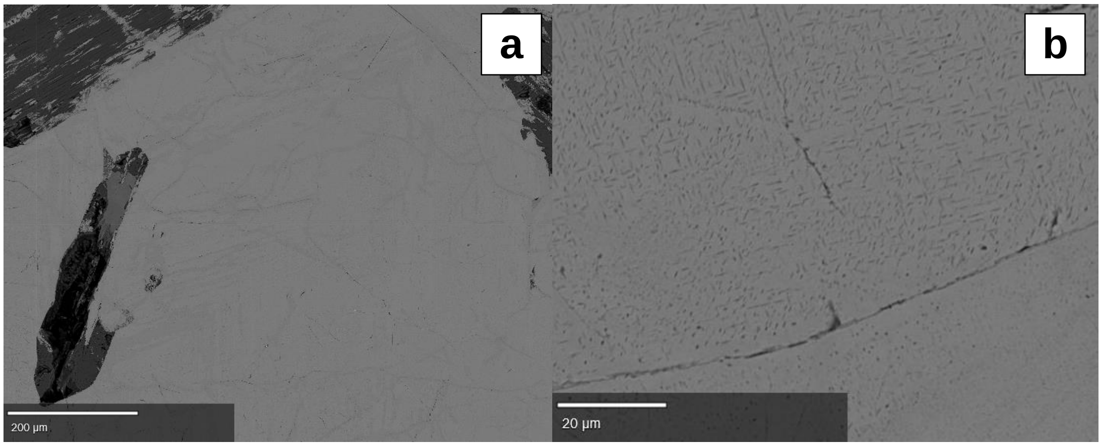

Figure 16: *BSE images of exsolution lamellae in sample EL-BM-02.*

Throughout the sample (see figure 16), the magnetite (Mgt) matrix has many lines with a different BSE contrast in various shapes and patterns such trellis texture with an increase in titanium content. These may be ilmenite exsolution lamellae of the ilmenite-hematite solid solution. However, as Ti is low in this sample, this texture may be the result of magnetite to maghemite conversion. The surface has many cracks which seem to follow the orientation of the laminae. Some of the zoning (see figure 16a and 17a) is irregular and could have formed from alteration.

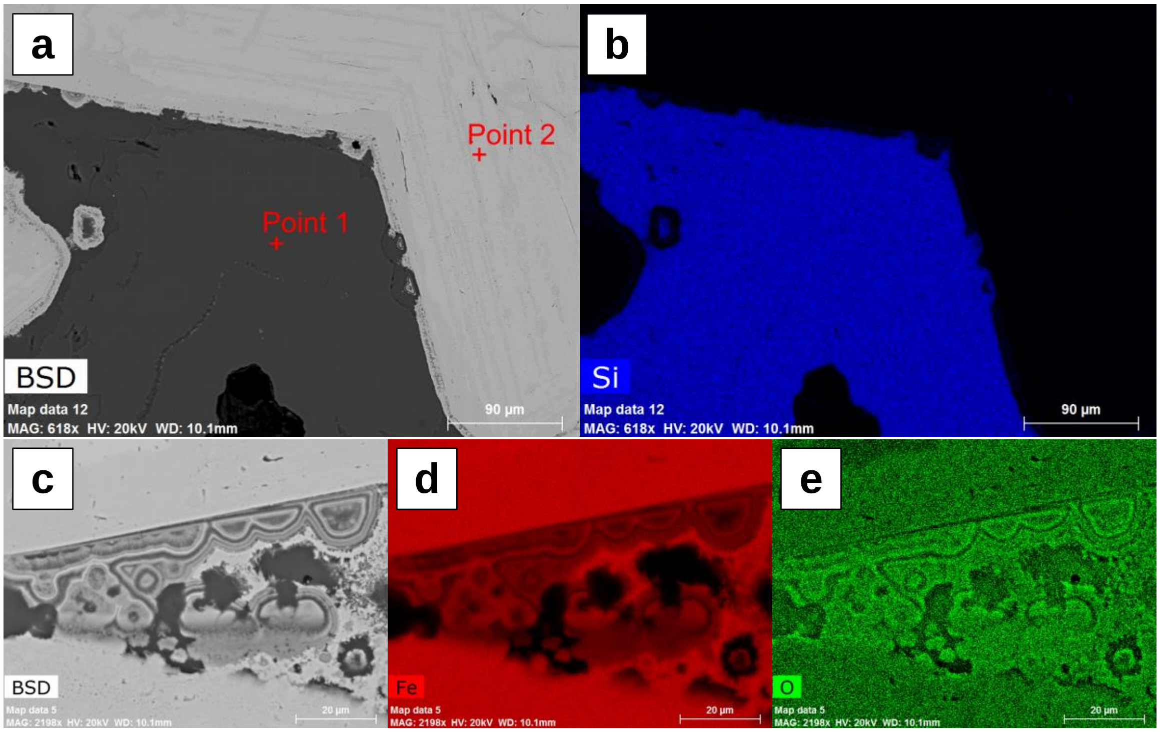

Figure 17: *Images taken by SEM of secondary minerals and textures in EL-BM-02.*

Many of the voids seem to be filled with SiO_2 (quartz composition, see figure 17a & b, see Appendix) pseudomorphs, most of which show an abundance of colloform textures decorating the grain boundaries of the magnetite matrix (see figure 17c, d & e). This shows rather clear contrast, within the sample, between primary and secondary iron oxide.

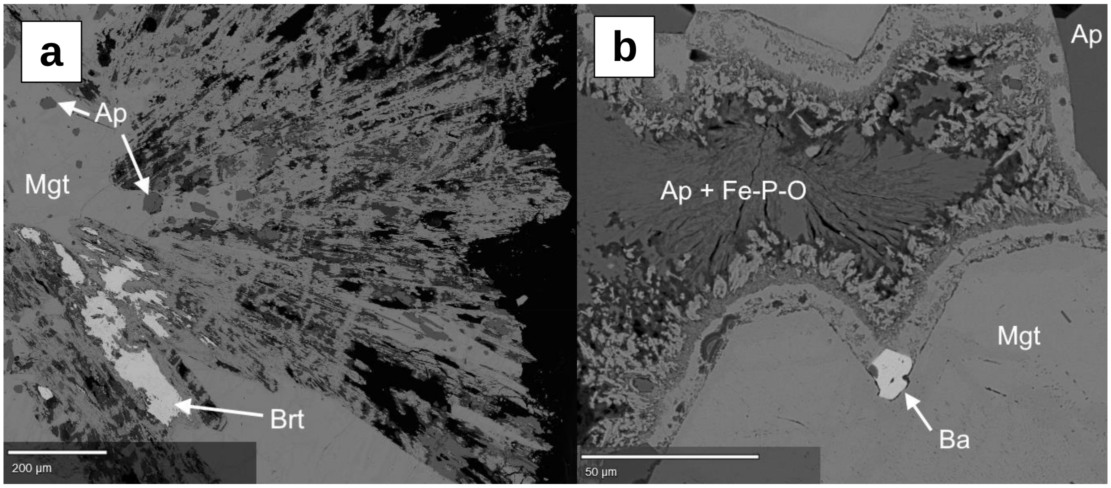

Figure 18: *BSE images of secondary morphologically constrained Baryte.*

There are also small grains of baryte ($BaSO_4$) that seem to be closely related to areas of alteration since it commonly occurs as distorted aggregates within the aforementioned alteration textures (see figure 18 or see waypoints 8 and 17 on the online BBV export for more context). In addition, there are "vestigial" and somewhat skeletal alteration-induced structures: such as the baryte (Brt) and other accessory minerals taking on the shape of large needles.

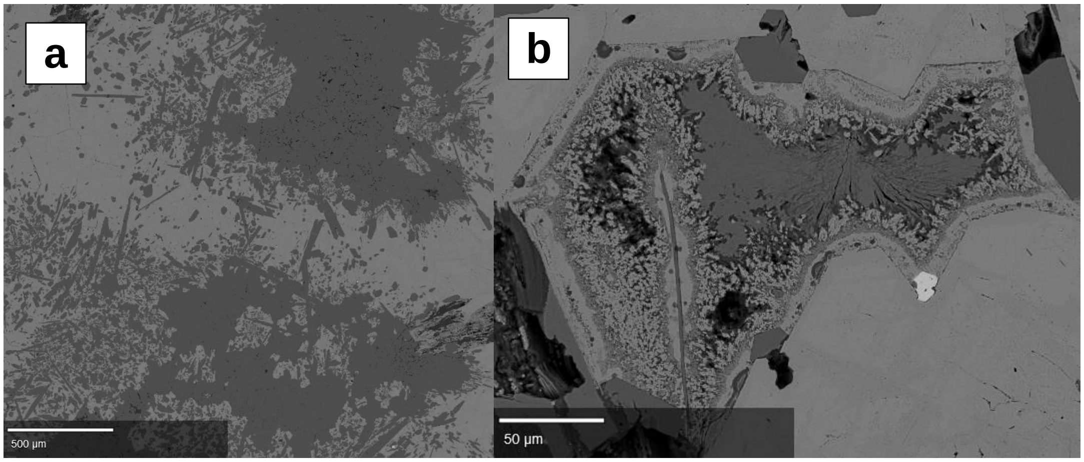

Figure 19: *BSE images of apatite splays and complex secondary textures.*

Also, there are many patches or rather splays of apatite crystals (see figure 19), randomly oriented that seem to crosscut the large needles growths. The baryte seems to be related to an alteration process. As shown in the figure 18b and 19b above, the grain is restricted to the available intergranular space it formed in and takes shape within cavities areas or along with the heavily altered apatite crystals, such as in figure 18a.

Sample EL-JM-82

The thin section prepared for this sample focuses on the magnetite vein seen in the andesite hand sample. The ochrous matrix is revealed to be jarosite (light grey in figure 20) with many larger grains of K-feldspar and quartz.

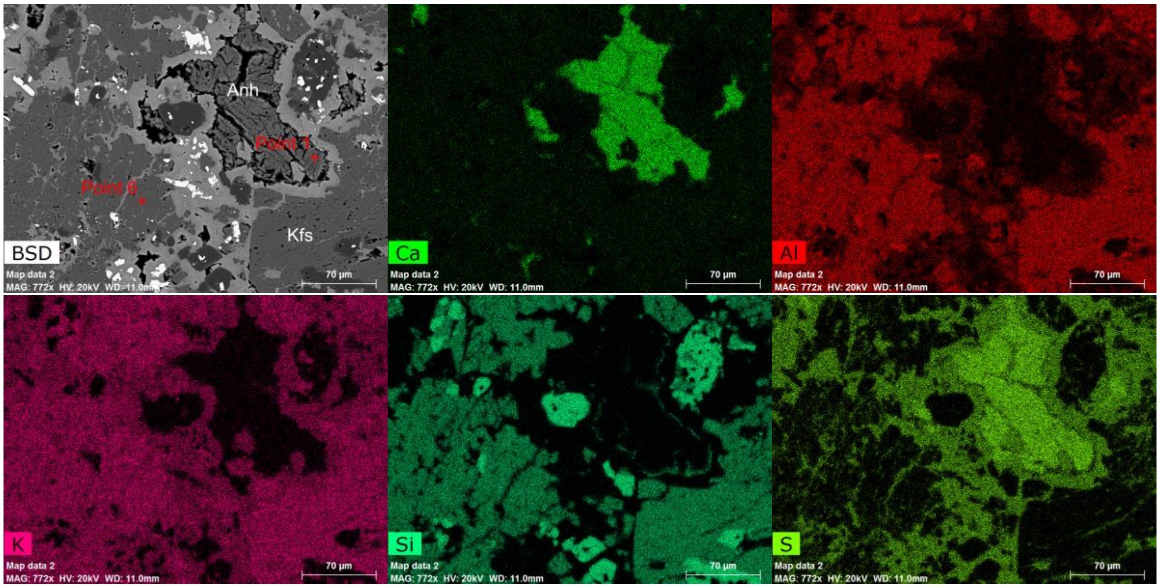

Figure 20: *An BSE image and EDS maps showing select mineral compositions.*

The EDS maps in figure 20 show rounded to subangular silicate (dark grains in BSE) grains with many smaller inclusions. These have been identified as K-feldspar (Kfs) confirmed by EMPA and EDS (see map 2, pt. 6). The much darker grains in BSE, near black, are of silicate composition, predominantly as quartz. The cracked irregularly shaped grain is anhydrite (Anh, see map 2, pt. 1), showing strong signs of alteration and its texture is not shared with other phases within the sample.

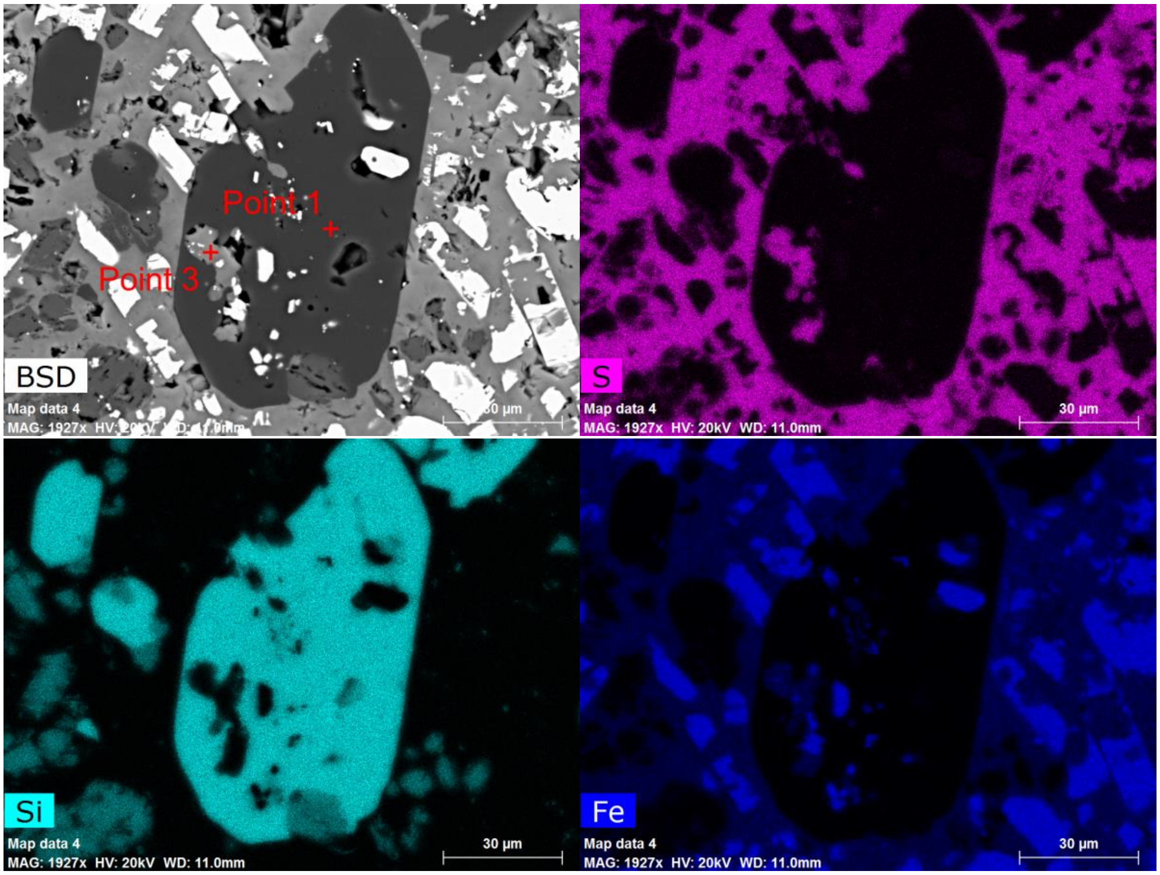

Figure 21: *An BSE image and EDS maps showing rounded quartz with inclusions.*

There are small but bright inclusions in the BSE image of figure 21. These are primarily incomplete euhedral Fe oxide crystals, likely either magnetite or hematite. These partially grown crystals along with the silicate grains (Qtz, see figure 21, map 4, pt. 1) are floating within a matrix of a relatively mixed composition: the matrix (map 4, pt. 3) has strong EDS signals of S, Si, Al, K, Fe and O.

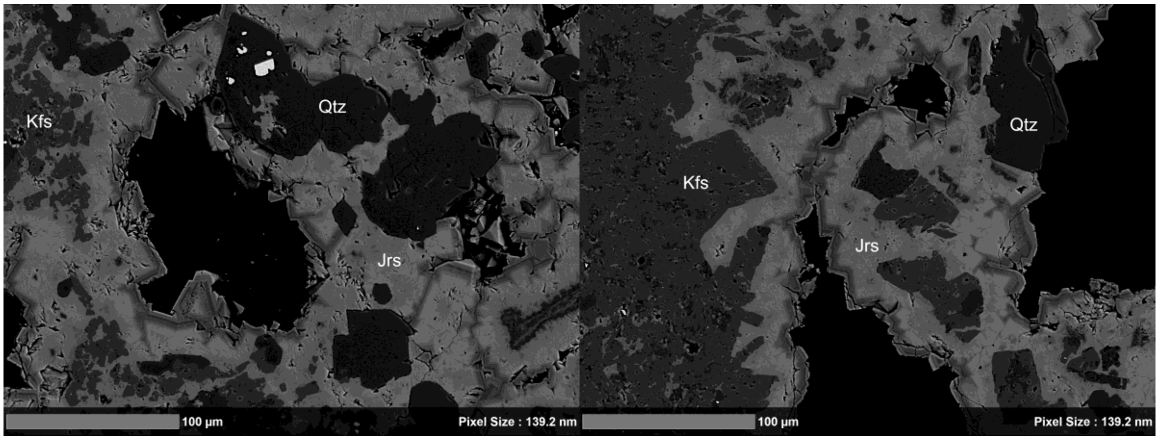

Figure 22: *BSE images of well-defined zoning in jarosite along the sample's cavities.*

The matrix is mostly jarosite (Jrs) and possibly alunite (or *vice versa*) in sharply defined zoned areas around intergranular cavities (see figure 22), likely from hydrothermal fluids passing through (Velasco & Tornos, 2012) and possibly some traces of mica. There are trace amounts of titanium throughout the sample, but of relatively unchanging composition in the overall interstitial material except for the magnetite vein. In contrast to the other samples, no Fe-P-O or apatite was observed within this sample.

Sample EL-JM-P4

This sample is an epoxy mount of unconsolidated granular Fe-P-oxide material. The same sample was presented by Mungall et al. (2018) as an example of quenched pyroclastic material.

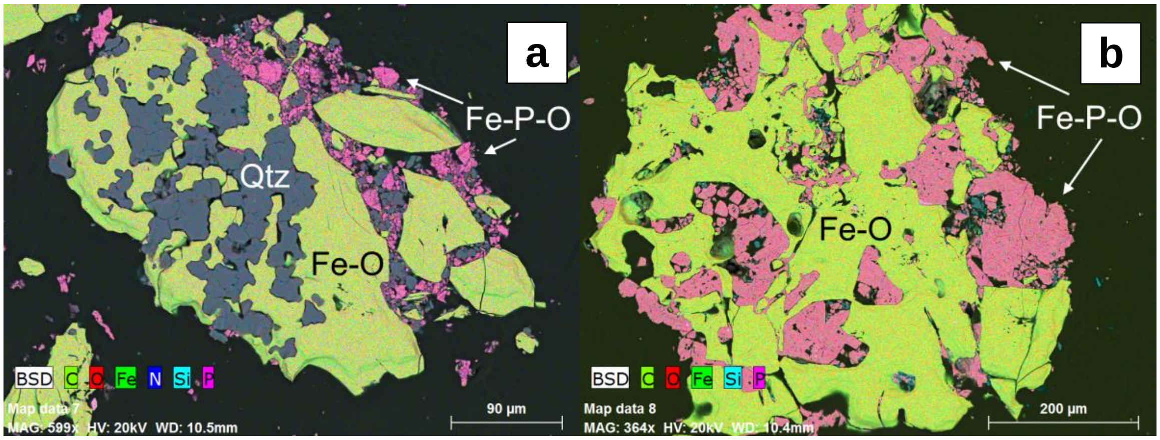

Figure 23: *Composite EDS images showing "lava lamp"-like textures.*

In figure 23a, an EDS composite map (7) with very dark lava-lamp-like features of almost pure Si-O (quartz-like, Qtz) composition as confirmed with the microprobe. This same composition was found in other samples also such as EL-JM-82, EL-BM-02, etc. The lightly coloured "yellow green" (false colours) material is Fe oxide, and the small granular "pink" grains are a mixture of broken pieces of Fe-P-O, Si-O, and Fe-O. There are weak Al and S signals throughout the sample which are likely from minor accessory minerals possibly from weathering. Figure 23b and 24a show similar textures except the globules are Fe-P-O hosted in a Fe oxide matrix.

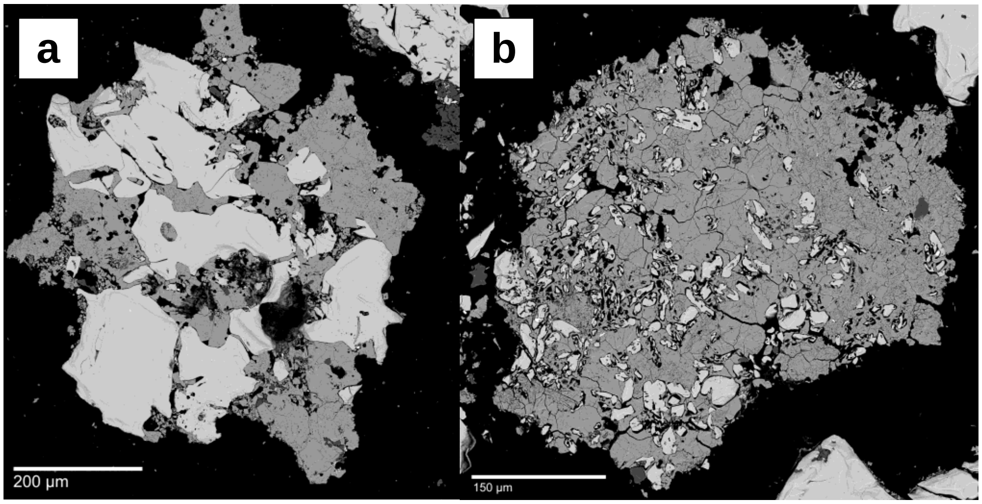

Figure 24: *BSE images of "lava lamp" and emulsion-like textures.*

This sample contains a profusion of iron phosphate, which can be observed throughout the entire sample. Grains such as shown in figure 24b (waypoint 19 in BBV) are irregularly distributed and are rounded grains of magnetite within a larger grain of iron phosphate. This texture is emulsion-like, as if these were immiscible liquids.

Figure 25: *BSE images of small REE mineral grain aggregates.*

Some of the iron oxide host grains have accessory REE minerals that were observed using EDS (see figure 25, map 11 and 14), such as xenotime (rare) and monazite-(Ce) (more common throughout sample). However, these were too small for the microprobe to obtain consistent and valid results. Thus, the point data obtained are not included here. That being said, the data did confirm strong signals for REE content such as Y and Dy for xenotime, and Ce, Gd, Nd with trace amounts of Ca in monazite-(Ce). All of these REE grains have uneven irregularly shaped outlines and are smaller than 10 µm across. These minerals seem to be spatially related (commonly occur together) with the Fe-P-O except for xenotime.

Sample EL-BM-01

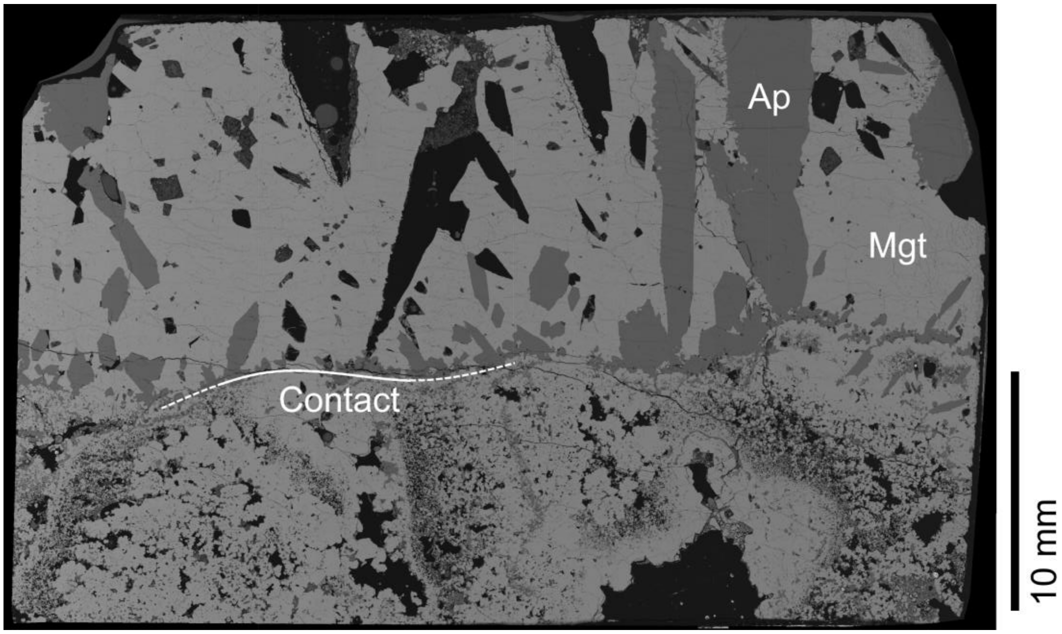

Figure 26: *BSE image of the EL-BM-01 thin section with a sharp contact.*

This thin section (see figure 26) focuses on the contact that was visible in the hand sample. The outer part of the crustiform contact containing the large (within the order of cm) fluorapatite (Ap) crystals has a magnetite (Mgt) matrix that is massive and coherent. The apatite crystals are perpendicular to sub-perpendicular to the contact surface. On the opposite side, the matrix is more granular, more porous; the minerals are significantly smaller and are in seemingly random orientations.

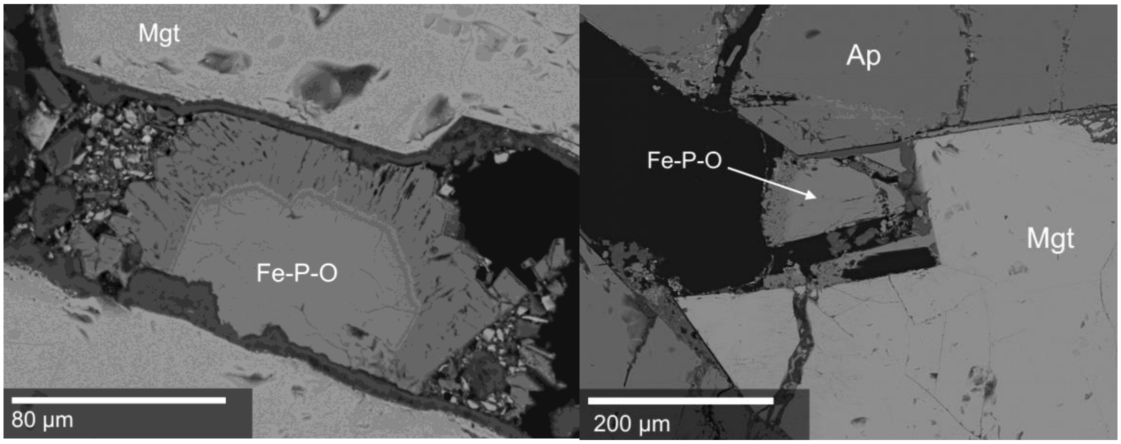

Figure 27: *BSE image of secondary Fe-P-O near the contact in EL-BM-01.*

In comparison with other samples, Fe-P-O is rare and is restricted to cavities and areas of alteration appearing as a secondary phase like in figure 27 (or see waypoints 8 and 9 on the online BBV export for more context) which is closely located to the contact. Apatite grains range from subhedral to anhedral and are smaller than the Fe-P-O grains, most being less than 90 µm in diameter. There is also small angular material of quartz composition within the cavities. As all of these phases seem to be cavity-filling material within this part of the contact, these are most likely accessory or rather secondary phases. That said, this could be a separation or immiscibility texture, implying that apatite may be a primary phase. Along the contact area, some space-filling silica is found with small crustiform textures, possibly from later alteration. However, no silica or quartz is found with the massive half; it seems to be restricted to the granular half.

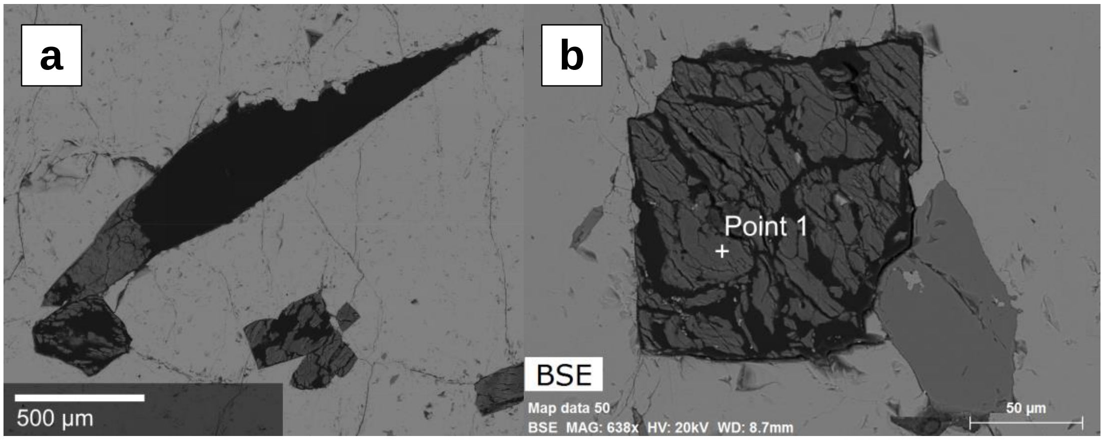

Figure 28: *BSE images of secondary smectite clays in EL-BM-01.*

Many of the large cavities observed within the massive half are from apatite crystals that have been weathered out or likely plucked out as the specimen was cut (see figure 28a), and now partly filled with a clay-like alteration mineral (figure 28b, map 50). This material is the same as the clay-like material pseudomorph after pyroxene. Chamosite is unlikely as there are near-equal proportions of Fe and Al and contains too much Si. These are likely Fe-rich smectite clays such as nontronite or saponite replacing diopside (Velasco & Tornos, 2012). It seems restricted to the massive half within this sample. In addition, there is magnetite within these cavities that was possibly reprecipitated, mixed and intergrown in close relation to the mentioned alteration phases.

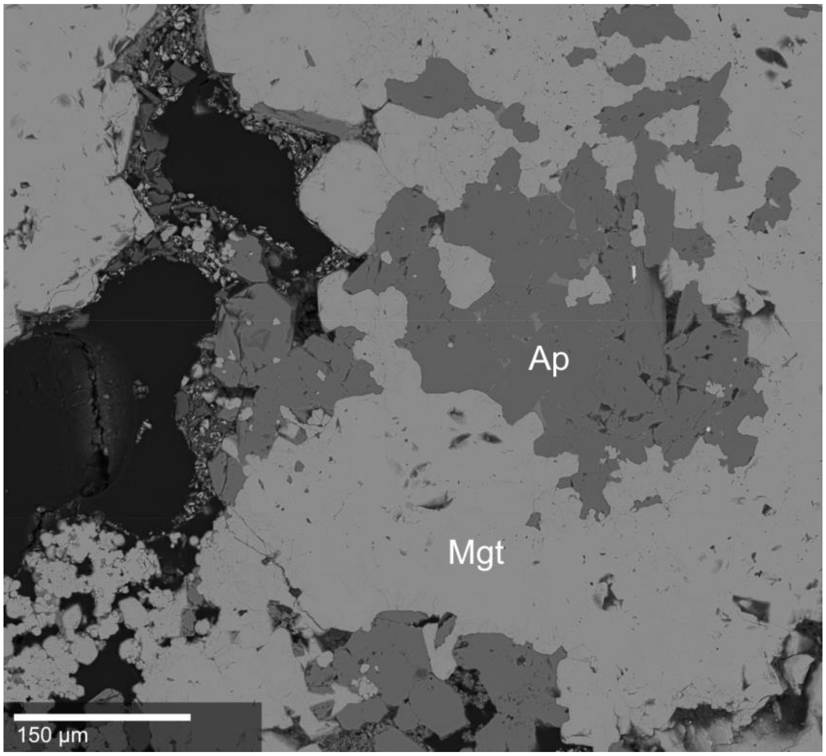

Figure 29: *BSE image of apatite splays in the granular half of EL-BM-01.*

Similarly to sample EL-BM-02, patches or splays of apatite aggregates have been observed with the granular half (see figure 29) in contrast to the large euhedral apatite crystals found along the contact; these are subhedral to anhedral and are much smaller in comparison.

Sample EL-BM-03

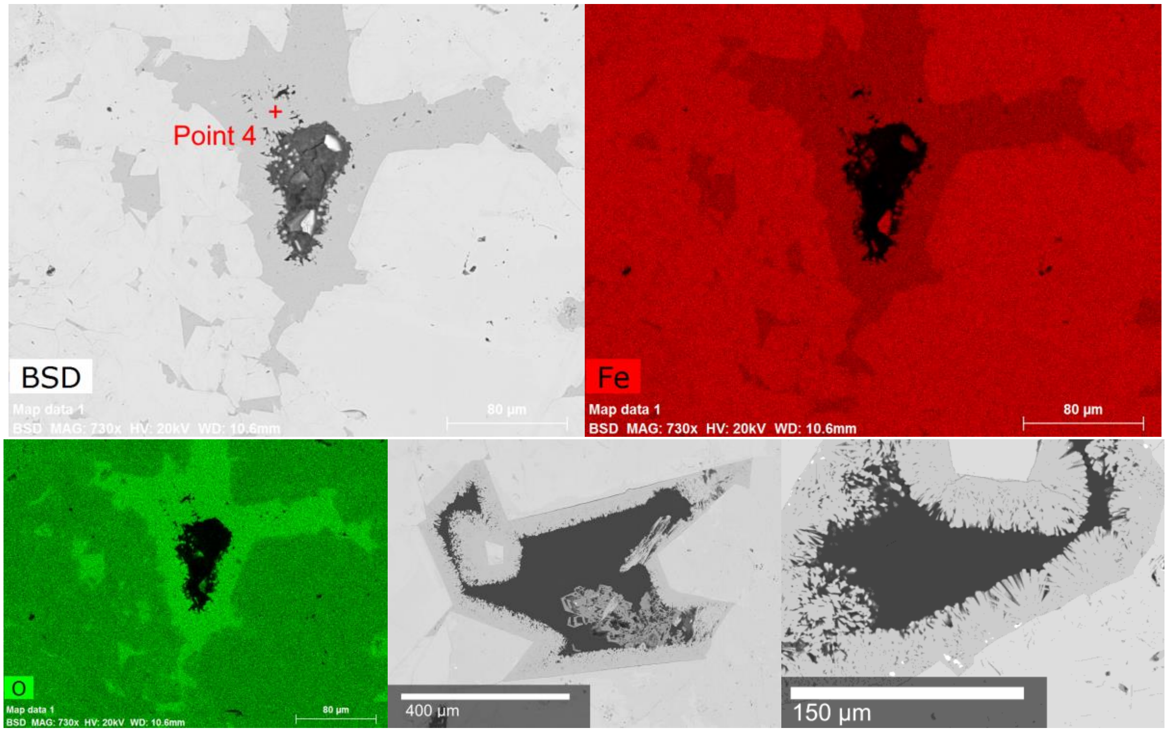

Figure 30: *BSE and EDS composite images of altered Fe oxide in EL-BM-03.*

This diktytaxitic magnetite sample has an abundance of small vugs filled with altered iron oxide (possibly hematite or goethite – higher O to Fe ratio) rounded needles (see figure 30, map 1, or waypoint 3 and 4 in the BBV export). Many of these cavities are found throughout the sample but are completely filled; this texture is quite common within this sample.

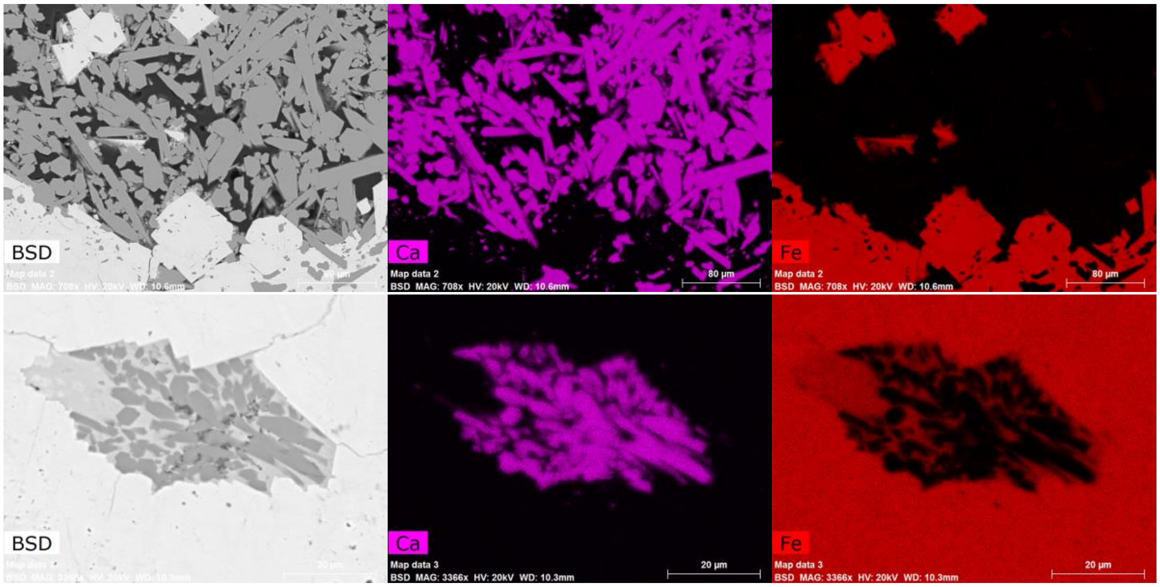

Figure 31: *BSE and EDS composite images of filled cavities in EL-BM-03.*

Many of the partially filled cavities (see figure 31, map 2 and 3) are also filled with euhedral to subhedral aggregates of apatite with little amounts of interstitial secondary silicate minerals. Many similar cavities are filled with these apatite crystals floating within an altered iron oxide matrix.

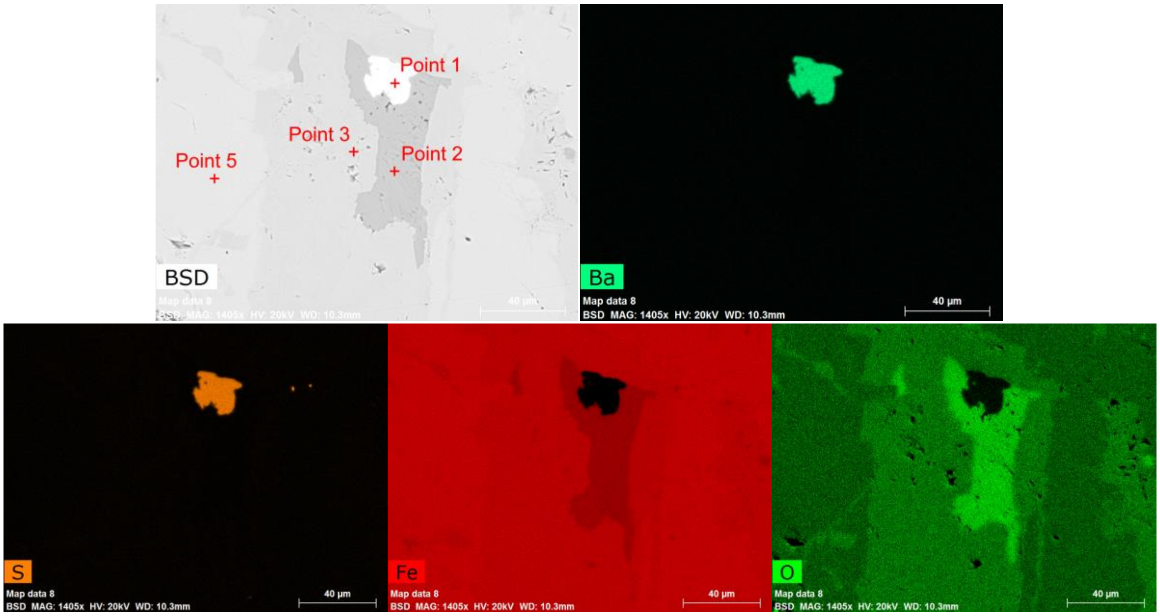

Figure 32: *BSE and EDS composite images of baryte and Fe oxide in EL-BM-03.*

However, some of these filled cavities have a weak signal of P within the altered iron oxide phase. It is possibly an intermediate phase between apatite that had filled the cavity and the surrounding magnetite. This specific filled cavity (see figure 32, map 8) has three phases: shown by the different levels of contrast within the iron oxides, with increasing oxygen content, and decreasing iron content perhaps indicative of a change from hematite to magnetite. At the core, there is a bright grain of baryte (map 8, pt. 1). This is possible evidence of hydrothermal alteration after most of the magnetite within this sample had already crystallised. Interestingly, the baryte has a low oxygen response in this EDS map.

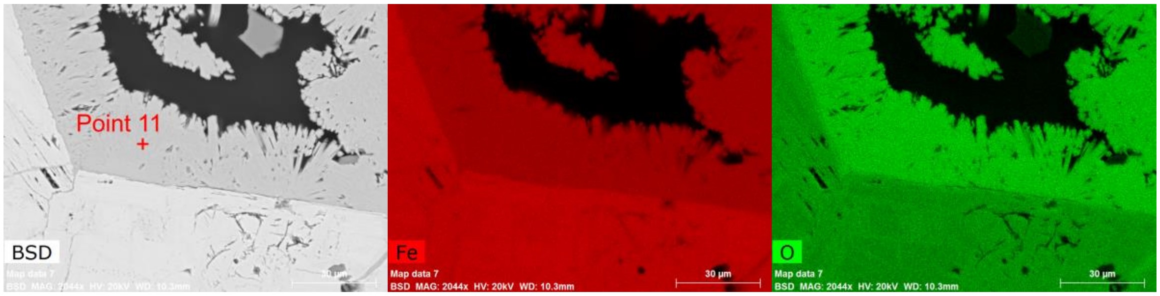

Figure 33: *BSE and EDS composite images of secondary Fe oxide in EL-BM-03.*

In map 7 (see figure 33 or waypoint 4 in the BBV export), better exposure of these cavity-filling iron oxide needles is observed, along with it in the upper centre is a subangular piece of apatite. Part of these needles show a centre of nucleation, possibly taking advantage of the cracks along the magnetite grain boundaries. These are likely iron oxy-hydroxide considering the higher O:Fe ratio and botryoidal growth habit.

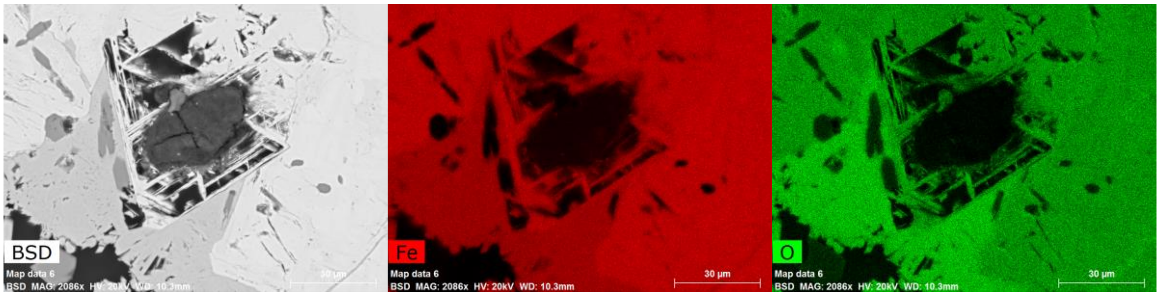

Figure 34: *BSE and EDS composite images of secondary Fe oxide in EL-BM-03.*

Nearby (see figure 34, map 6), sharp growths of iron oxide needles can be observed around a darker grain that seems to be aluminum silicate, possibly clay minerals.

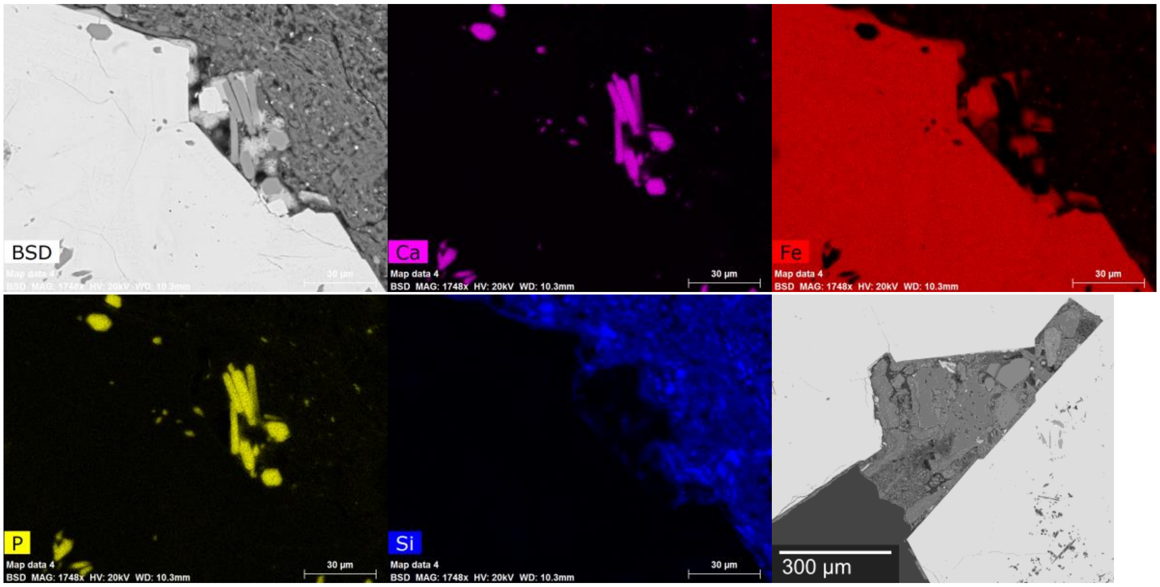

Figure 35: *BSE and EDS composite images of secondary textures in EL-BM-03.*

In map 4 (see figure 35 or BBV export waypoint 3), part of a cavity that is filled with aluminium silicate platy material and small angular pieces of iron oxide and apatite, arranged in a fashion that is similar to a debris flow or mud flow on a smaller scale. This secondary material occurs in various shapes and size. However, these could be fillings from sample preparation. In addition, there are a few euhedral to subhedral crystals of apatite floating within this. Along these crystals and along the grain boundaries of the magnetite matrix are small (see figure 36 for a larger example) spherulitic growth of iron oxide. These are secondary or rather reprecipitated phases, possibly hematite or goethite in light of its higher oxygen to iron ratio (in comparison to the primary magnetite).

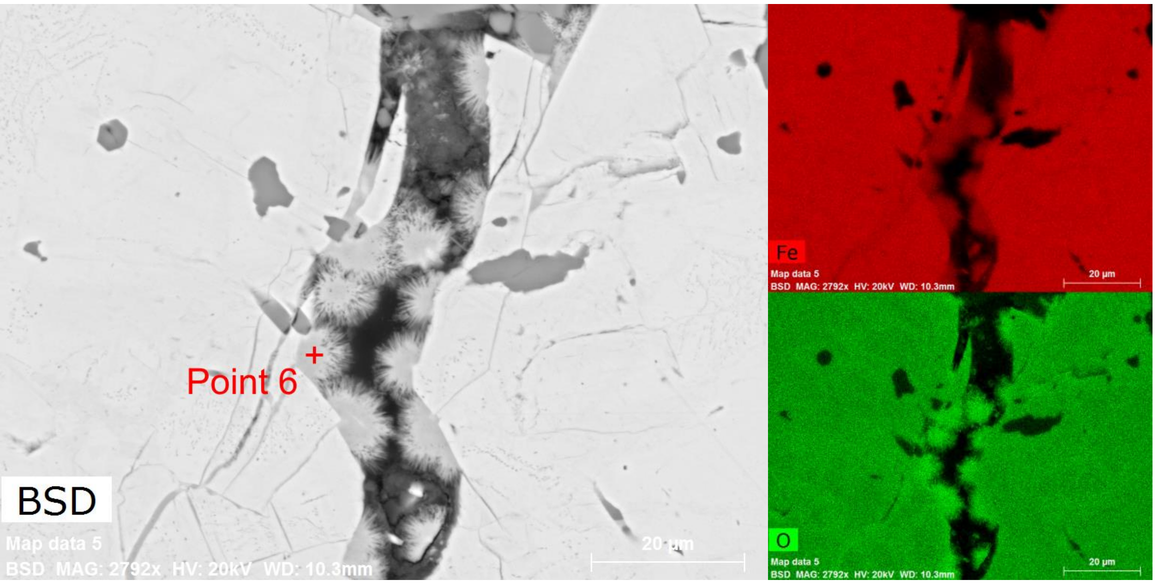

Figure 36: *BSE and EDS composite images of Fe oxide spherules in EL-BM-03.*

Close by is map 5 (figure 36) where these needle spheres, likely goethite due to its habit of stellate growth in acicular aggregates, are better formed within a crack that is less than 15 µm wide. All of these seem to preferentially nucleate along grain boundaries rather than on their own (such as nucleating on intergranular phases). They are on average ~ 8.5 µm in diameter. Along this fissure, there are also roundish anhedral grains of apatite that are likely in deformed shapes either from non-suitable crystallization conditions (such as weak temperature gradients) and or from alteration processes.

Sample EL-BM-04

The “columnar” magnetite has yet to be analysed with SEM. The following observations are primarily based on reflected light microscopy (RL). Superficially, this sample is similar to sample EL-BM-03, with the exception that the cavities observed here are generally rounder, fewer and somewhat are interconnected. However, this sample is more cracked and brittle; the shape of the cracks and cavities is dictated by the magnetite columnar growths (that are perpendicular to the thin-section plane) following a rough honeycomb-like pattern as mentioned earlier.

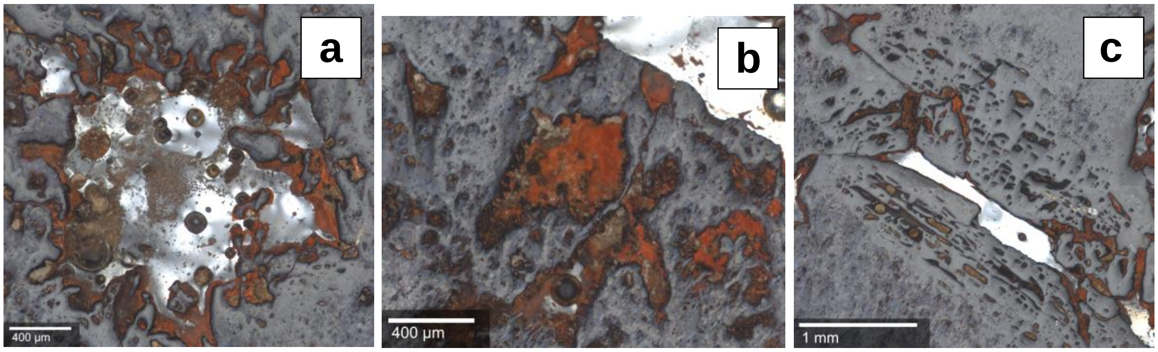

Figure 37: *RL images of different features (waypoint 1,2,3 in BBV export) in EL-BM-04.*

Very fine-grained material is observed (see figure 37a), 15 µm or less in size, that is possibly phyllosilicate-like material as seen in sample EL-BM-03 (as both samples share similarities and were both collected from the same area). Conversely, these could also simply be fine fragments of the surrounding reddish brown material that is likely to be a mixture of heavily altered apatite and hematite infilling cavities found within the primary magnetite. Figure 37b is a magnified view on the interstitial material. The crystal habit is completely obscured, it has uneven translucency, and its shape is completely dictated by the cavities it fills. On multiple occurrences, it seems that most of the elongate cavities occur parallel to “column” boundaries (see figure 37c). This suggests a possible timing relationship between the infilling brown material and the column boundaries of the sample; the infilling material was possibly later reshaped after its emplacement.

Sample EL-JM-11

This thin section was obtained from a previous study (Mungall et al., 2018) along with the hand sample EL-JM-11 that was collected at Laco Sur. An image mosaic produced with ATLAS 5 has revealed many different features and a phase such as monazite-(Ce) with secondary cavity-filling structures, possibly dendrites of Fe oxide surrounded by a spheroidal overgrowth of Fe-P-O.

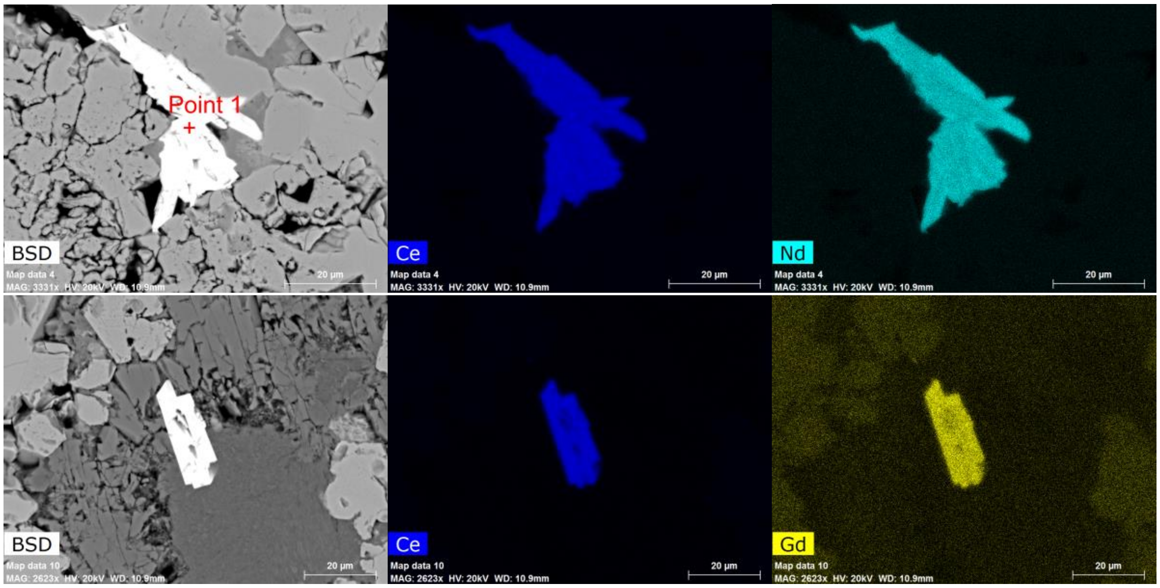

Figure 38: *BSE and EDS images of monazite-(Ce) in EL-JM-11.*

We observe REE-rich grains (figure 38, map 4 and 10, or waypoint 1 and 6 in BBV export), most of which are less than 30 µm in diameter: these have retained their shaped and are both morphologically and chemically monazite-(Ce). Although some samples have a considerable amount of monazite-(Ce), REE mineral grains such as the ones shown in figure 38 were relatively sparse in sample EL-JM-11.

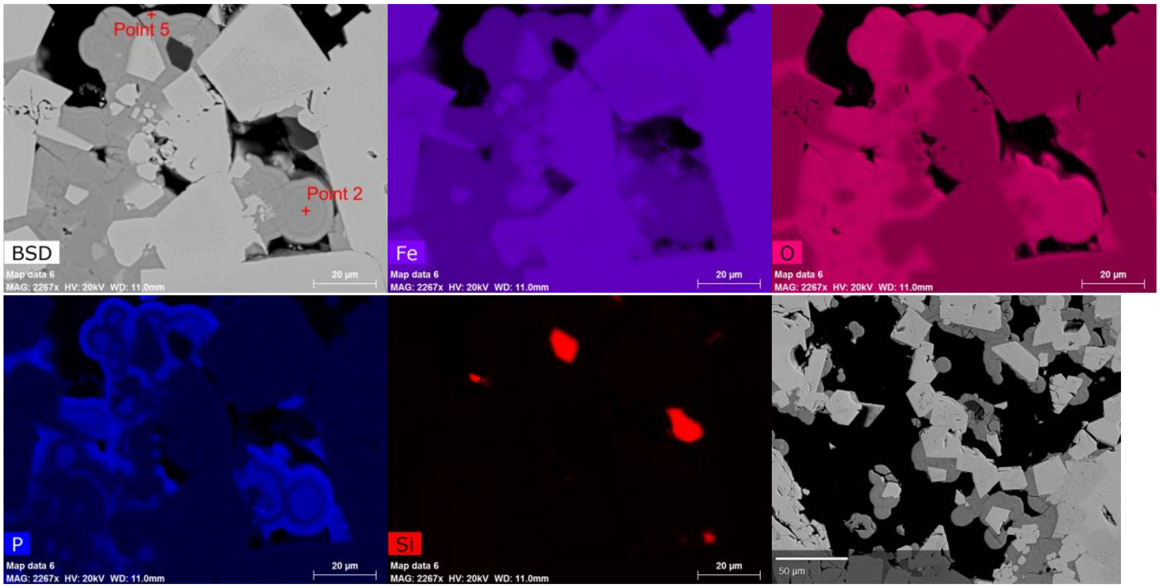

Figure 39: *BSE and EDS images of botryoidal Fe-P-O in EL-JM-11.*

Iron phosphate appears in botryoidal growths (see figure 39, map 6 or waypoint 9 in BBV), with traces of Cu, Mg around its outer edges, and reprecipitated iron oxide along grain boundaries in the sample's cavities.

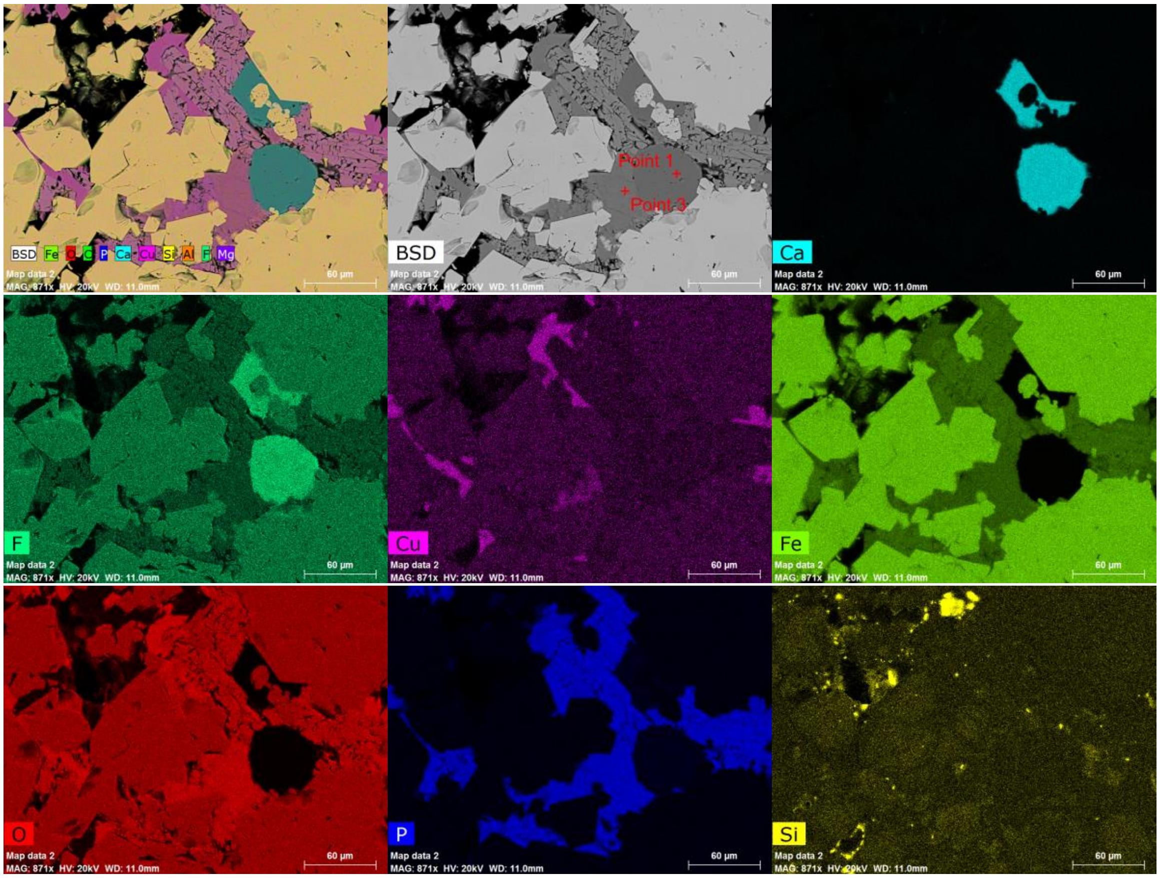

Figure 40: *BSE and EDS images of fluorite and Fe-P-O in EL-JM-11.*

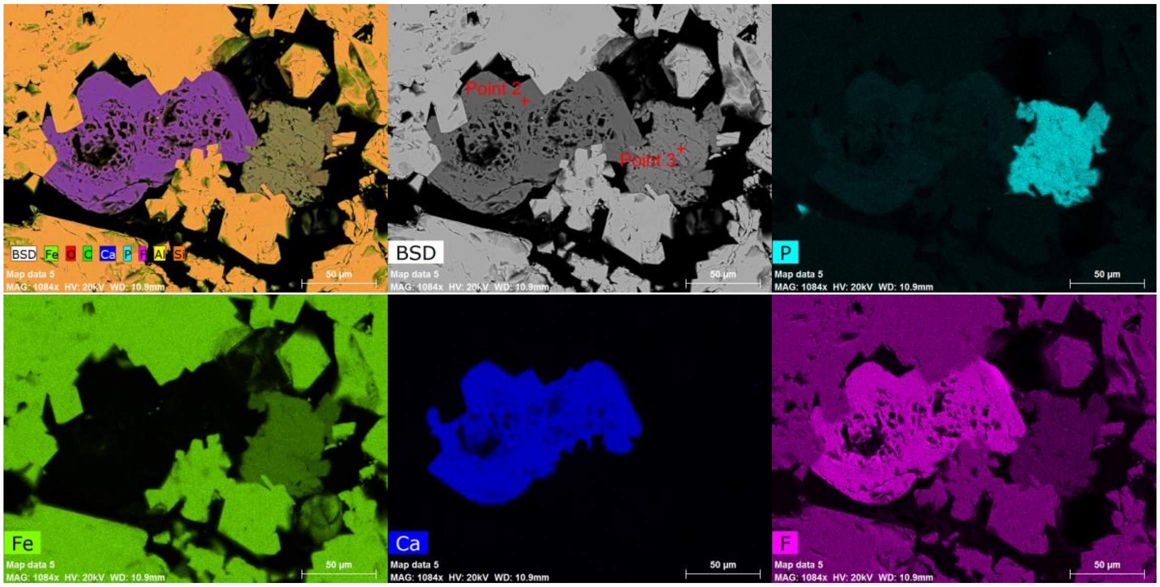

Figure 41: *BSE and EDS images of fluorite and Fe-P-O in EL-JM-11.*

The intergranular space is filled with secondary Fe-P-O and possibly fluorite (see figure 40, 41, map 2 and 5 pt. 2) based on EDS analysis. The iron phosphate phase seems to be a late phase as it appears only interstitially, among the magnetite grains. Some of the secondary phases contain small concentrations of copper (see figure 40).

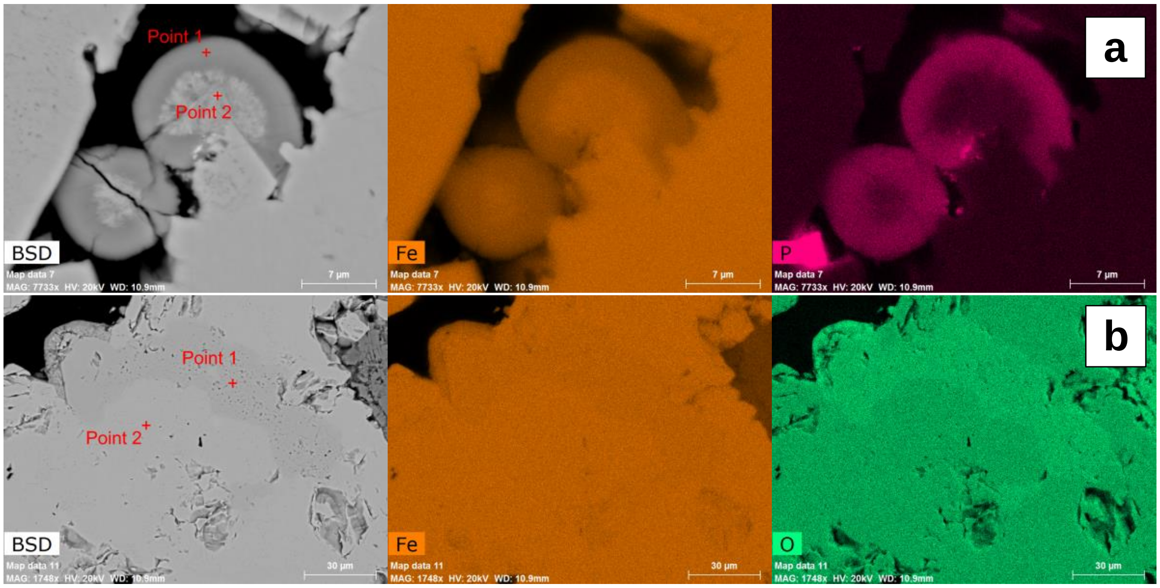

Figure 42: *BSE and EDS images of botryoidal Fe-P-O in EL-JM-11.*

Botryoidal growths of Fe-P-O can be observed throughout the sample (see figure 42, 43, map 7, 11 and waypoint 12 in BBV); the fine needles in the core that are less than 2 µm across individually arranged in spherules: this occurs as Fe-O (on the inner part), Fe-P-O (outer) and crustiform growth along the grain boundaries of magnetite grains.

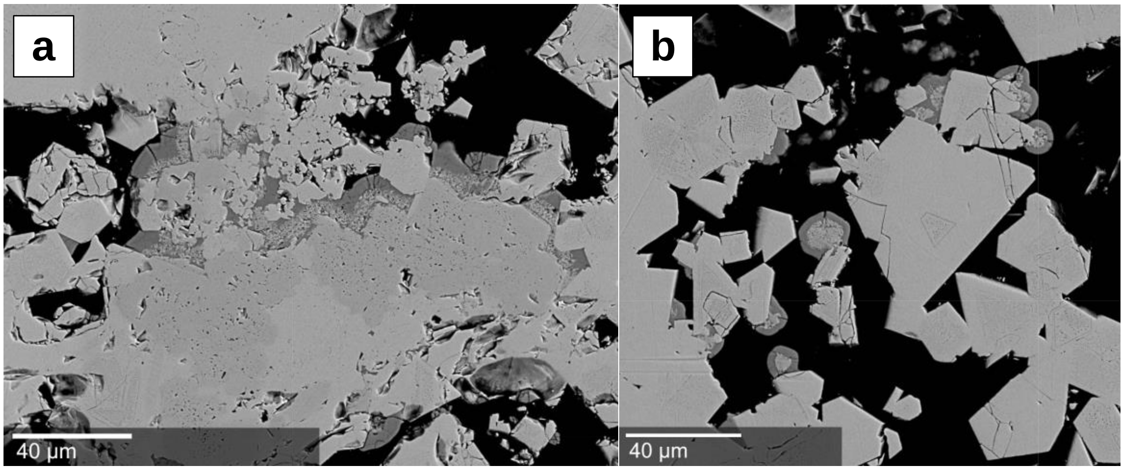

Figure 43: *BSE and EDS images of botryoidal Fe-P-O in EL-JM-11.*

In addition, we can observe a “seeped” or stain-like texture (see figure 42b, 43a), slightly darker and more porous patches within the consolidated magnetite grains. These secondary phases and textures are likely a result of precipitation of the magnetite or alteration by hot fluids through dissolution.

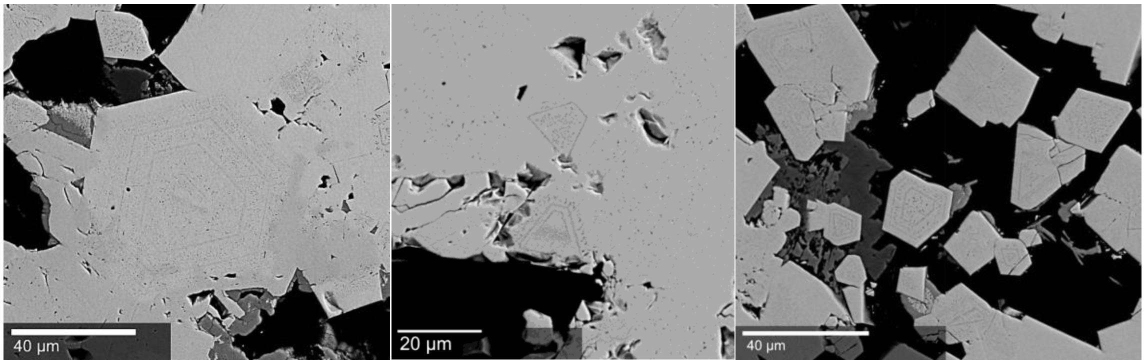

Figure 44: *BSE images of “zoned” euhedral magnetite grains in EL-JM-11.*

Throughout the sample we can see many magnetite grains with textural zoning (see figure 44, map 8 or waypoint 2, 11 in BBV), taking on the hexoctahedral shape of the magnetite host grain. However, with the EDS compositional map (see figure 45), the “zoning” is revealed to reflect nano-sized Ca-Mg-Si-rich inclusions and likely not oscillatory zoning (due to its staccato-like or rather disjointed nature). The pattern obtained in map 8 (see figure 45) in particular is very complex as it exhibits multi-generational inclusions: primary, and similarly to fluid inclusions, there are secondary and even pseudo-secondary (healed fractures) textures. Additionally, the larger diamond-shaped grain (figure 45), which encompasses two separate groups of zoning likely formed by nucleating at connecting apexes from two smaller engulfed magnetite grains. There are many occurrences of this well-defined zoning in magnetite grains (such as the one shown in figure 44) that include what appears to be domains with a large number of these inclusions. Most of these are distributed along growth zones making them very likely identifiable as primary inclusions. In order to observe this feature in greater detail, a euhedral magnetite grain (see figure 46) with similar well-defined zoning but somewhat less complex pattern was chosen to be examined through 3D FIB-nanotomography.

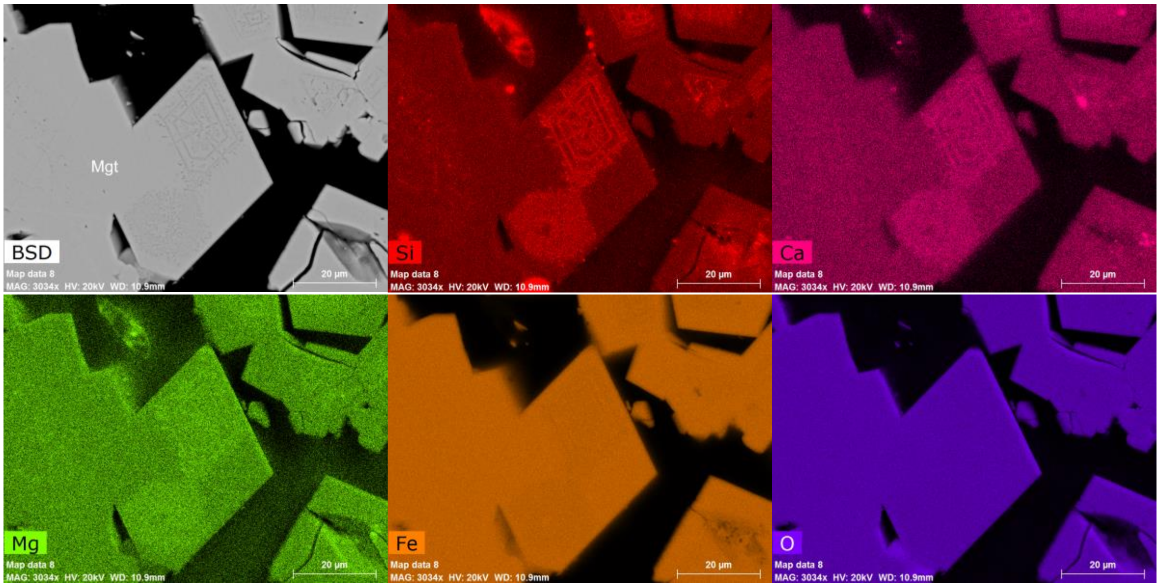

Figure 45: *BSE and EDS images of Ca-Mg-Si nano-inclusions in EL-JM-11.*

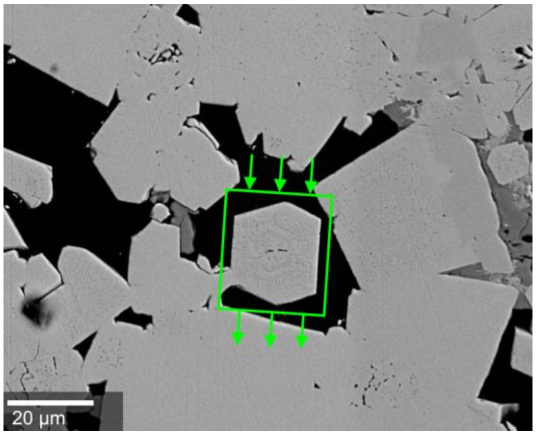

Figure 46: *BSE image of the targeted grain for 3D FIB-nanotomography in EL-JM-11.*

The green box (see figure 46) outlines the FIB milling target of about 34 µm by 32 µm. The arrows depict the FIB milling direction. The images shown in figure 47 are selected slices from the ATLAS 3D FIB-nanotomography run that was conducted revealing that the zoning is in fact composed of nano-scale inclusions and not voids. Farther towards the middle of the grain, slices reveal polymineralic (possibly melt) inclusions which might not have been visible with conventional SEM imaging. Particularly in slice #3151, the inclusions enclosed fit in a “jigsaw” like or rather an interlocking pattern of rounded grains wrapping around one another (see figure 47b for a magnified view).

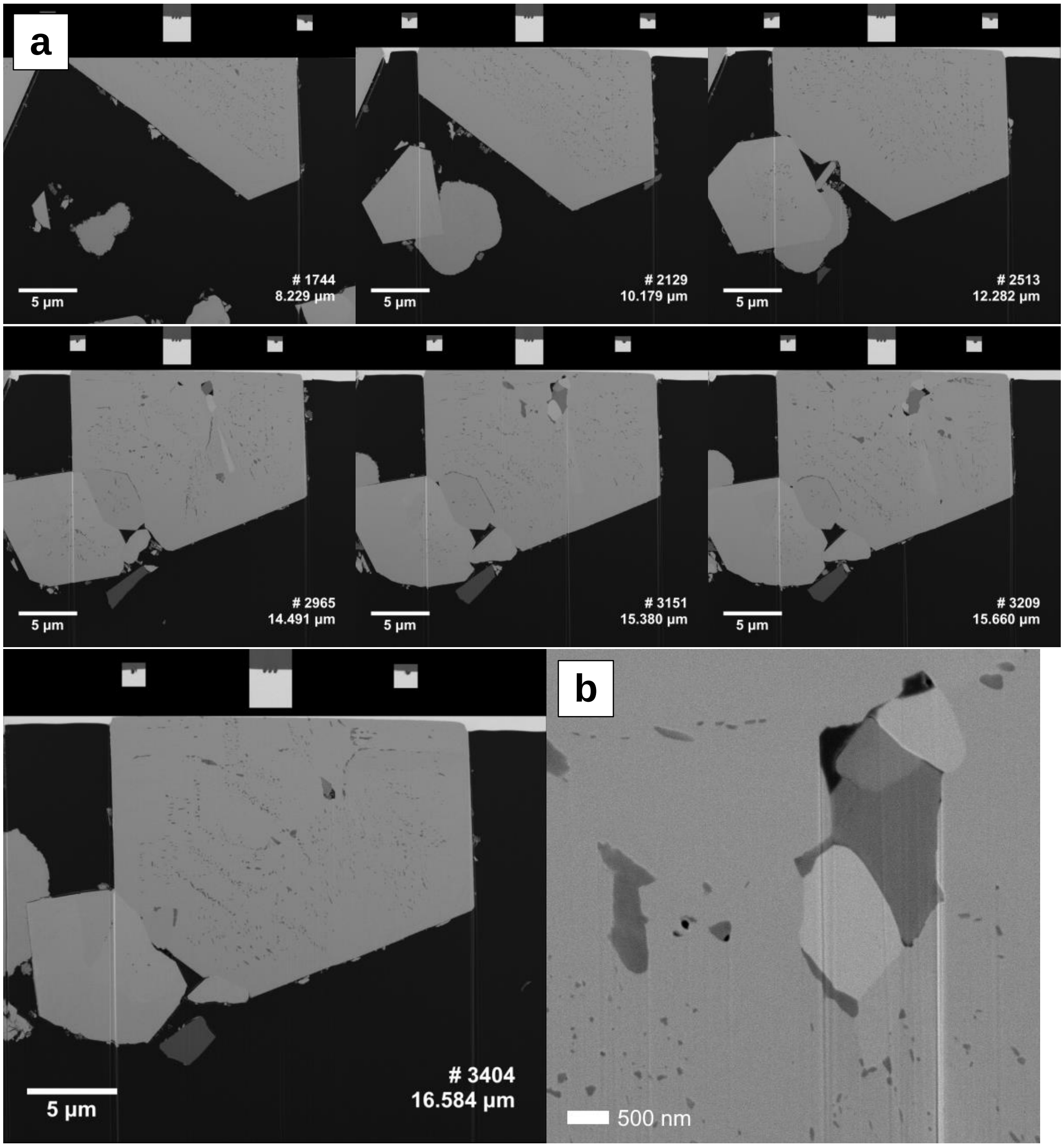

Figure 47: *FIB images of select slices from the ATLAS 3D FIB-nanotomography run.*

There are other phases as well that have yet to be confirmed. As mentioned before, the compositional EDS map revealed the inclusions to be predominantly a Ca-Si-Mg phase, possibly diopside which is part of the primary El Laco mineral assemblage.

Discussion

Mineral Assemblage

The mineral assemblage (see Table 5) is primarily iron oxide in different forms (magnetite, hematite or possibly maghemite) which was observed in all samples.

Table 5: Individual sample mineralogy

Sample	Minerals and approximate modal abundances
EL-BM-01	Mgt/Hem (90%), Ap (10%), FP (trace), Qtz, Sm
EL-BM-02	Mgt/Hem/Mgh (95%), Ap (5%), FP (trace), Qtz, Brt
EL-BM-03	Mgt (97%), Ap (3%), Qtz (trace), Brt, FH, Gt
EL-BM-04	Mgt/Hem (98%), Ap (2%)
EL-JM-11	Mgt/Hem (99%), FP (trace), Qtz, Fl, Mnz,
EL-JM-82	Jrs (45%), Kfs (35%), Qtz (12%), Mgt/Hem (7%), Anh (1%), Aln (trace)
EL-JM-P4	Hem/Mgt (96%), FP (4%), Qtz (trace), Mnz, Xnt

Acronyms used: Ap: apatite, Aln: alunite, Anh: anhydrite, Brt: baryte, Fl: fuorite, FH: iron oxyhydroxide, FP: iron phosphate, Gt: goethite, Mgh: maghemite, Mnz: monazite, Hem: hematite, Jrs: jarosite, Kfs: K-feldspar, Mgt: magnetite, Qtz: quartz, Sm: smectite, Xnt: Xenotime.

Iron phosphate (Fe-P-O) was found in almost all samples: EL-BM-01, EL-BM-02, EL-JM-P4 and EL-JM-11. However in EL-JM-11, its occurrence seems more coherent: they are instead cracked less rounded blocky grains with sharper edges unlike the other samples. Apatite was found in sample EL-BM-02, -01, -03 and possibly BM-04. It is interesting to note that apatite does not always appear everywhere; this could imply that P is not a necessary substance for the magnetite mineralization observed in some of the samples. Quartz was equally observed in almost all samples: EL-JM-82, -11, -P4, EL-BM-01, -02, -03, and possibly EL-BM-04. Different sulphates were found such as baryte in EL-BM-02, -03, and anhydrite in EL-JM-82. Because of where and how they appear, they are likely secondary phases that were brought in hydrothermally, possibly in some kind of saline fluid; baryte and anhydrite are commonly morphologically constrained by primary features (see figure 18, 20 and 32). On that same note, REE minerals were identified and likely formed hydrothermally: monazite-(Ce) (observed in EL-JM-P4 and

EL-JM-11) seemed related to secondary Fe-P-O emplacement, and possibly deformed xenotime (which only occurs in EL-JM-P4) on the contrary seem unrelated to iron phosphate; it was possibly a primary phase. Fluorite was identified only in EL-JM-11, but its presence could play a role as a flux as it commonly reduces viscosity in melts hence the name (derived from *fluere* in Latin). Clay-like minerals, possibly smectite clays such as nontronite or saponite, were found in EL-BM-01, and likely also appear (in a different form) in EL-BM-03 and EL-BM-04. Other alteration phases include the high O:Fe ratio phases (see figure 33 and 36) which could be a polymorph of Fe_2O_3, goethite and iron oxyhydroxides. And as expected out of all the samples, EL-JM-82 is the most unique in terms of mineral assemblage as it is the only andesite sample and has a minor amount of Fe oxides comparatively; the main differences are jarosite which has been observed in a similar context (Tornos et al., 2017), K-feldspar, possibly alunite (around the zoned cavities in jarosite, see figure 22) and the lack of iron phosphate.

Textures and Distinguishing Features

In samples EL-BM-01, -02, -03, EL-JM-11, and EL-JM-82, there are many small sporadic round voids (0.5 to 2 µm in diameter) seemingly unrelated to zoning such as the examples discussed in figures 44, 45 and 46: these could be solution pits or vesicles, as these are also found within the incomplete iron oxide crystals “floating” in a jarosite-K-feldspar matrix (EL-JM-82). These could be larger analogues of the nano-scale melt inclusions in EL-JM-11. Ilmenite exsolution with a weak to moderate trellis texture was observed in sample EL-BM-02, but not as well formed as in recent work (Ovalle et al., 2018) that showed a clear increasing trend of Ti content with depth based on observations from deep core samples (> 150 m). Ilmenite mostly occurs in igneous and metamorphic rocks, and as these exsolution lamellae are found in primary magnetite (in relatively unaltered states), it is very likely to be igneous in origin. Sample EL-BM-03 also shares similar “zoning” or laminae textures in iron oxide, possibly as exsolved illmenite. Columnar magnetite (such as EL-BM-04) has previously been observed (Henriquez & Martin, 1978) and is thought to be a rare rapid-growth texture diagnostic of a magmatic origin (Nyström & Henriquez, 1994). In sample EL-BM-01, -02, -03, radiating splays of apatite occur within the larger cavities of the samples: likely apatite occurs both as a primary and secondary (in this case) phases; in sample EL-BM-02, very clear Fe-replacement of euhedral apatite crystals was observed. As apatite is susceptible to hydrothermal alteration, it is likely there was an event with localised Fe-rich fluids (possibly in part from the magnetite) after the primary magnetite and apatite had already crystallised. A key feature is the well-defined Ca-Mg-Si “zonings” or “droplets” observed in EL-JM-11: similar ones have been previously observed (Dare et al., 2015). However, FIB 3D FIB-nanotomography has revealed that these are in fact micro- to- nano-scale melt inclusions (possibly of diopside-like composition). These were possibly overgrown by its magnetite crystal host. One of the best evidences for an immiscibility separation relationship that requires the least amount of interpretation is the occurrence of glassy globules in rocks of different composition (Bowen, 1928): glassy quartz globules were observed in nearly all samples. That being said, molten silica may be out of the question because of the high temperatures that would be involved. In addition, there are melt-like textures in sample EL-JM-P4 such as the Fe-P-O, emulsion texture of Si both occurring in iron oxide, and even the reverse with iron oxide in Fe-P-O. Conversely, iron oxide was observed in an altered form as radial growths in EL-BM-03: these possibly formed at an earlier event or the same event that brought an influx of aluminum silicates platelets. Moreover, the other Fe-P-O form occurring as small rounded secondary growths in cavities could have formed from iron oxide bathing in a P-rich fluid or from open-space filling solute-rich vapour. The largest and most unique texture is the megaspherulites in EL-BM-02: similar samples have been observed before at Laco Sur (Henriquez & Martin, 1978) and Cristales Grandes (Tornos et al., 2017). These range from ~ 0.5mm to 5.5 cm in diameter. Spherulites seem to occur from growth-front nucleation (GFN): secondary nucleation from quick cooling (such as quenching) of a heterogeneous liquid in chemical disequilibrium (Gránásy et al., 2005). How are the spherulites in EL-BM-02 formed? As one possibility, there was primary diopside that was altered due to hydrothermal processes where the magnesium and calcium components have been removed. However, no evidence of primary diopside was observed within this sample. Another possibility is that apatite may have grown in spheres comprising very thin needles within the magnetite incidentally causing the magnetite to form these spherulitic shapes. However, since the dominant phase is magnetite and not apatite, the magnetite should be dictating the growth, meaning apatite crystallizes interstitially and is rather elongate because of rapid growth (likewise for the magnetite). Something, such as quenching of an iron oxide melt, may have caused the magnetite to have this shape; successively apatite grew interstitially.

It is interesting to note that the BM sample series has undergone more alteration since they contain abundant secondary features and were collected from unconsolidated deposits. The JM series was selected to be as fresh as possible, which gives us something that would be closer to primary textures. For example, we can infer the tephra sample (EL-JM-P4) is not affected by weathering or heavy alteration as it lacks the features like botryoidal iron oxyhydroxides and smectite clays that are common in the BM series.

Reactions and Trace Elements

In an older study on Kiruna-type deposits, Frietsch (1978) mentioned an intimate relationship between IOA deposits indicated by an enrichment of Ba (mostly in the form of baryte), while late-stage hydrothermal ores are depleted in trace elements. If any genetic model is to work for El Laco, it should also work for other IOA deposits such as Los Colorados (Chile), Cheever Mine (NY, USA), or even Kiirunavaara (Sweden) itself. Dare et al. (2015) proposed hydrothermal magnetite by replacement and that the textures are pseudomorphs of igneous textures. Mg and Mn concentrations in the magnetite mineralization should be equal or higher than its host rock (andesite in this case) if it were hydrothermal (Dare et al., 2014). However, their presented geochemical data shows an average trend that is equal or significantly lower than both the altered and unaltered host rock.

As for immiscibility, shoshonites are normally not Fe-rich to the extent of Kiruna-type or IOA deposits. That being said, they have defined characteristics, some of which are a high Fe_2O_3/FeO ratio and low iron enrichment (Morrison, 1980). If El Laco involves “shoshonitic” immiscibility for its mode of origin, it should be verified by measuring the ratios and if possible, sampling andesite with evidence of unusual iron-enrichment trends (generally not expected but could have led to the formation of an immiscible iron oxide melt). As an Fe-melt would require high temperatures, F, Cl, P, Si could act as a flux for iron oxide (Taylor & Owen, 1993; Tornos et al., 2016).

The presence of maghemite along with high temperature phases could entitle for an alternative mode of origin of the magnetite. Qualitatively, hematite or rather Fe_2O_3 forms at lower temperature and or higher oxygen pressures than magnetite (Parkinson, 2016). However, the presence of phosphate (binds strongly to Fe oxide surfaces) or silica (significant effect on sorption and recrystallization of Fe oxides) inhibits the dissolution-precipitation path to hematite, and instead promotes the metastable maghemite (Taylor & Owen, 1993). Sample BM-02 has anomalous magnetic domains; magnetite has a very low remanence and coercivity meaning it does not retain its “magnetic permanence” for prolonged periods. And thus, the genesis of naturally “magnetised” (as in aligned domains) magnetite, also known as lodestone, is uncertain. It is likely that some of the non-magnetic iron oxide is hematite or some other little to not magnetic mineral. Maghemite is a polymorph of Fe_2O_3 that is very strongly magnetitic: ferromagnetic. It is possible that all three occur in small quantities within this sample, which would explain the distinct magnetitic domains. It also forms a series with magnetite (inverse spinel) and has a similar crystal structure, a defect spinel (Parkinson, 2016). As both are spinel-group minerals, maghemite arises by the high-temperature oxidation of magnetite. Diffusion alone is enough to explain the kinetics needed to change magnetite to maghemite by oxidation (Sidhu et al., 1977): magnetite nanoparticles can be transformed into maghemite and hematite by dry oxidation with relative ease. However, this is dependent of the precursor materials’ morphology and particle size. Those with larger initial size transform directly to hematite (Khan et al., 2015). Taylor & Owen (1993) have presented the following possible reactions:

$$4\,Fe_3O_{4(s)} + O_{2\,(g)} \rightleftharpoons 6\,Fe_2O_{3(s)}$$

$$4\,Fe_3O_{4(s)} + 6\mathrm{x}\,H_2O_{(l)} + O_{2\,(g)} \rightleftharpoons 6\,Fe_2O_3 \cdot \mathrm{x}\,H_2O_{(s)}$$

Gibbs energy differs by $\Delta_r G°$ as a stoichiometric multiples (x) of this reaction:

$$\alpha\,Fe_2O_{3(s)} + \mathrm{x}\,H_2O_{(l)} \rightleftharpoons Fe_2O_3 \cdot \mathrm{x}\,H_2O_{(s)}$$

These reactions show that hematite is the preferential final oxidized form as opposed to its metastable maghemite counterpart, whether it involves dry or hydrated oxidation. It is also suggested that certain iron hydroxides and oxyhydroxides contain additional anions that may affect equilibrium. McElhinny & McFadden (2000) say maghemite is the ultimate a low-temperature oxidation or weathering product of magnetite. However, as magnetite does transform to maghemite at a low temperature, it is likely that the transformation would be more efficient at a high subsolidus temperature. Modeling the magnetite to maghemite conversion as f(O_2) increases, will prove useful in explaining remnants of magnetic domains of what used to be solid end-member magnetite. Tornos et al. (2017), mention that between ca. 800° and 100°C, liquid water was not present making it unlikely for hydrothermal alteration as the iron ore cooled (a vapor would not be able to transport the amount of Fe present at El Laco). This is based on oxygen isotope data, fluid inclusion data and thermodynamic constraints. As mentioned earlier, the oxidation of magnetite to maghemite (both spinel-group minerals) does not need to involve H_2O (Khan et al., 2015). On the other hand, it does involve O at a high temperature.

Geologic models and processes

Possible Sources of Iron

One hotly debated idea is an Fe-melt originating from deep within the Earth’s crust (Dare et al., 2015; Mungall et al., 2018). However, strong evidence for this is yet be discovered. A proposed source is the potential of iron formations within the volcanic basement. Alternative means of formation of Fe-C-P-O liquids could be from direct melting of phosphatic carbonate-facies iron formation due to magmatic underplating by mafic magma. Although phosphatic carbonate-oxide ironstones receive little attention in the geological literature because the presence of P makes them unattractive as iron ores, they occur worldwide in deposits ranging from Archean to Recent in age with regional extents and thicknesses locally reaching hundreds of metres (Bekker et al., 2010; Li et al., 2013; Young, 1977). Silurian phosphate-rich oolitic ironstones in beds up to 15 m thick occur about 200 km east of El Laco in the Central Andean Basin (Astini & Marengo, 2006; Conti et al., 1995) and may have correlatives beneath northeastern Chile (Tornos et al., 2011). Below the El Laco volcano, Tornos et al. showed (in 2016) multiple older layered volcanic complexes atop one another, and below is a late Miocene breccia pipe above an ignimbrite basement (~4 to 10 Ma) over an andesite sequence (~9 to 12 Ma) and finally a siliciclastic sedimentary basement at the very bottom. They also suggest a possible iron source to be an Ordovician-Silurian 10 km thick sedimentary sequence as a basement hosting abundant ironstones and discontinuous layers of iron- and carbonate-rich phosphorites.

Models

Somma volcano model: On the topic of the Somma volcano model presented in the introduction, a more recent study by Naranjo et al. (2010) looks at drill core samples provided by Compañía Mineria del Pacífico (CMP). These were carefully studied leading to the identification of at least seven different stratovolcanoes, with a central dome structure (Pico Laco) within a central crater. Moreover, metasomatic alteration was observed to have increasing intensity with depth likely caused by volatile-rich fluids exsolving from an Fe oxide liquid.

Hydrothermal model: This proposed model (Dare et al., 2015; Rhodes et al., 1999; Sillitoe & Burrows, 2002) primarily looks at the metasomatism of the andesite by “magnetite-precipitating fluids” as a part of the sequence of complete replacement of the andesite lava flows to magnetite by hydrothermal alteration through “dissolution of the silicate minerals and precipitation of magnetite” (Dare et al., 2015). Oscillatory zoning of Si-Ca-Mg within the magnetite has been interpreted as fluctuating fluid composition or physio-chemical conditions.

Tornos et al. suggested (in 2017) magmatic magnetite and a superheated hydrothermal system: They do not dictate a specific model of choice *per se* (they do mention the following flotation model), but rather that the mode of origin should involve a combination of magmatic and hydrothermal processes.

Efficient magmatic-hydrothermal flotation of magnetite suspensions: This model from Ovalle et al. (2018) invoked for magnetite accumulations at the surface through transport by fluidization of magnetite clusters and buoyancy from exsolved $FeCl_2$ (Knipping et al., 2015) bubbles nucleating on the magnetite crystals (that originated from a crystal-mush within an andesitic magma chamber) that was seeped through from an underlying mafic magma. Although the authors proposed an interesting and plausible process, such a mechanism fails to account for the variety of textures such as the megaspherulitic texture in the EL-BM-02 specimen. More work is needed on the characterization of the minerals, even iron oxide itself: if maghemite is involved, it could lead to a different mode of origin.

Conclusion

The ATLAS 5 toolkit and workflow have provided efficient means to image and navigate through entire samples: this combined system of hardware, software and suite of techniques has allowed us to provide a seamless correlation of images of large areas from the macro-scale to the nano-scale and the tools to assist in the visualization of quantitative information. In addition to various observations in other samples, the target selected in sample EL-JM-11 for closer examination by FIB-SEM with ATLAS 3D has revealed new information. It has made visible the very small polymineralic inclusions exposing melt-like shapes that were previously not accessible. Otherwise, very fine features and textures such as the nano-inclusions could be misinterpreted as simple zoning or voids. This reveals how important large-area and higher-resolution (nano-scale) imaging really is. Many observations have been made as an attempt to answer the following questions:

1. Are melt inclusions confirmed or debunked?

  - The evidence is possibly convincing for most, but more work is needed.

2. Is it pervasive hydrothermal overprint or *hydrothermal-genic* mineralization?
    - Based on the present evidence so far, it is likely successive magmatic mineralization with multiple hydrothermal events.
3. Is the origin purely magmatic, hydrothermal, or a combination of processes?
    - Primarily magmatic likely from intense volcanic activity, but with a combination of hydrothermal-like events.
4. Are hydrothermal and magmatic magnetite characteristics well constrained?
    - The developed geochemical methods are for different rock types (not Fe-O dominated) and were not implemented with IOA deposits in mind. If a magmatic origin is proved, then the characterization needs to evolve to accommodate this deposit type.
5. If El Laco is magmatic, how are Fe-O or Fe-P-O melts produced? Can these melts form or erupt within the crust?
    - The answer could lie in the source of the iron. Iron formations are possibly too localised (any in Colorado or Sweden?). And, possibly successive deep magmatic events leading to a mafic iron-rich basement prove to be unlikely?

On-going and Future Work

As mentioned earlier, further work is needed, particularly on the current sliced images of EL-JM-11: these need to be aligned and processed with 3D modelling software such as ORS Dragonfly[5]. That said, a new grain should be targeted in order to reconstruct a 3D model with both compositional (EDS) and crystallographic (EBSD) information: this is needed to identify the phases at this scale. Unfortunately, the 3D EDS-EBSD work was not completed this time due to untimely technical issues and machine breakdown. Higher-resolution imaging (say 20 to even maybe 5 nm/pixel) could prove useful for areas of great interest. If the presence of “primary” maghemite could be documented, it would change the perspective of seeing it as a simple oxidation product for IOA deposits. XRD (x-ray powder diffraction) could help identify the different iron phosphates, iron oxides or oxyhydroxides, smectite clays and other unknown phases. Furthermore, TEM (transmission electron microscopy) could be used to see the crystal lattice of the iron oxides, Fe-P-O phases and iron oxyhydroxides to help identify these unknowns.

---

[5] See the following for more information: https://www.theobjects.com/dragonfly

References

Astini, R. A., & Marengo, L. F. (2006). Paleoambientes y estratigrafía secuencial de depósitos marinos marginales del Ordovícico de la sierra de Zapla (sierras Subandinas, noroeste argentino) y su relación con la Cuenca Andina Central. *Revista Geológica de Chile*, *33*(2), 247–276. https://doi.org/10.4067/s0716-02082006000200003

Bekker, A., Slack, J. F., Planavsky, N., Krapež, B., Hofmann, A., Konhauser, K. O., & Rouxel, O. J. (2010). Iron Formation: The Sedimentary Product of a Complex Interplay among Mantle, Tectonic, Oceanic, and Biospheric Processes*. *Economic Geology*, *105*(3), 467–508. https://doi.org/10.2113/gsecongeo.105.3.467

CAP Mineria. (2017). Annual Report 2017. Retrieved December 11, 2018, from http://www.cap.cl/cap/site/artic/20180329/asocfile/20180329161409/memoria_cap_sa__ingles___final.pdf

Conti, C. M., Rapalini, A. E., & Vilas, J. F. (1995). Palaeomagnetism of the Silurian Lipeón formation, NW Argentina, and the Gondwana apparent polar wander path. *Geophysical Journal International*, *121*(3), 848–862. https://doi.org/10.1111/j.1365-246X.1995.tb06443.x

Corona-Esquivel, R., Martínez-hernández, E., Henríquez, F., Nyström, J. O., & Tritlla, J. (2010). Palynologic evidence for iron-oxide ash fall at la perla, an oligocene kiruna-type iron ore deposit in northern Mexico. *GFF (Journal of the Geological Society of Sweden)*, *132*(3), 173–181. https://doi.org/10.1080/11035897.2010.519048

Dare, S. A. S., Barnes, S. J., Beaudoin, G., Méric, J., Boutroy, E., & Potvin-Doucet, C. (2014). Trace elements in magnetite as petrogenetic indicators. *Mineralium Deposita*, *49*(7), 785–796. https://doi.org/10.1007/s00126-014-0529-0

Dare, S. A. S., Barnes, S. J., & Beaudoin, G. (2015). Did the massive magnetite “lava flows” of El Laco (Chile) form by magmatic or hydrothermal processes? New constraints from magnetite composition by LA-ICP-MS. *Mineralium Deposita*, *50*(5), 607–617. https://doi.org/10.1007/s00126-014-0560-1

Frietsch, R. (1978). On the magmatic origin of iron ores of the Kiruna type. *Economic Geology*, *73*(4), 478–485. https://doi.org/10.2113/gsecongeo.73.4.478

Giannuzzi, L. A., & Stevie, F. A. (2005). *Introduction to Focused Ion Beams*. *Introduction to Focused Ion Beams: Instrumentation, Theory, Techniques and Practice*. https://doi.org/10.1007/b101190

Goldstein, J. I., Newbury, D. E., Michael, J. R., Ritchie, N. W. M., Scott, J. H. J., & Joy, D. C. (2017). *Scanning electron microscopy and x-ray microanalysis*. *Scanning Electron Microscopy and X-ray Microanalysis* (4th ed.). Springer. https://doi.org/10.1007/978-1-4939-6676-9

González Ferrán, O. (1974). International Symposium on Volcanology, Andean and Antarctic Volcanology Problems, 9-14 September 1974, Santiago, Chile (pp. 51–52). Santiago, Chile: International Association of Volcanology and Chemistry of the Earth’s Interior; Inter-Union Commission on Geodynamics; Pan American Institute of Geography and History.

Gránásy, L., Pusztai, T., Tegze, G., Warren, J. A., & Douglas, J. F. (2005). Growth and form of spherulites. *Physical Review E - Statistical, Nonlinear, and Soft Matter Physics*, *72*(1), 1–14. https://doi.org/10.1103/PhysRevE.72.011605

He, X. F., Santosh, M., Tsunogae, T., & Malaviarachchi, S. P. K. (2018). Magnetite-apatite deposit from Sri Lanka: Implications on Kiruna-type mineralization associated with ultramafic intrusion and mantle metasomatism. *American Mineralogist*, *103*(1), 26–38. https://doi.org/10.2138/am-2018-6254

Henriquez, F., & Martin, R. F. (1978). Crystal growth textures in magnetite flows and feeder dykes, El Laco, Chile. *The Canadian Mineralogist*, *16*(4), 581–589.

Henríquez, F., & Nyström, J. O. (1998). Magnetite bombs at el laco volcano, Chile. *GFF*, *120*(3), 269–271. https://doi.org/10.1080/11035899809453216

Hou, T., Charlier, B., Holtz, F., Veksler, I., Zhang, Z., Thomas, R., & Namur, O. (2018). Immiscible hydrous Fe–Ca–P melt and the origin of iron oxide-apatite ore deposits. *Nature Communications*, *9*(1). https://doi.org/10.1038/s41467-018-03761-4

Khan, U. S., Amanullah, Manan, A., Khan, N., Mahmood, A., & Rahim, A. (2015). Transformation mechanism of magnetite nanoparticles. *Materials Science- Poland*, *33*(2), 278–285. https://doi.org/10.1515/msp-2015-0037

Knipping, J. L., Bilenker, L. D., Simon, A. C., Reich, M., Barra, F., Deditius, A. P., et al. (2015). Trace elements in magnetite from massive iron oxide-apatite deposits indicate a combined formation by igneous and magmatic-hydrothermal processes. *Geochimica et Cosmochimica Acta*, *171*, 15–38. https://doi.org/10.1016/j.gca.2015.08.010

Leica Microsystems. (2014). Ion Beam Polishing of sample surfaces. Retrieved January 16, 2019, from https://www.leica-microsystems.com/fileadmin/downloads/Leica EM RES102/Application Notes/AN_EMRES102_Ion_Beam_Polishing_of_sample_surfaces_EN.pdf

Li, Y.-L., Sun, S., & Chan, L. S. (2013). Phosphogenesis in the 2460 and 2728 million-year-old banded iron formations as evidence for biological cycling of phosphate in the early biosphere. *Ecology and Evolution*, *3*(1), 115–125. https://doi.org/10.1002/ece3.443

McElhinny, M. W., & McFadden, P. L. B. T.-I. G. (Eds.). (2000). Chapter Two - Rock Magnetism. In *Paleomagnetism* (Vol. 73, pp. 31–77). Academic Press. https://doi.org/https://doi.org/10.1016/S0074-6142(00)80095-9

Morrison, G. W. (1980). Characteristics and tectonic setting of the shoshonite rock association. *Lithos*, *13*(1), 97–108. https://doi.org/https://doi.org/10.1016/0024-4937(80)90067-5

Mungall, J. E., Long, K., Brenan, J. M., Smythe, D., & Nasuland, H. R. (2018). Immiscible silicate and Fe-P oxide melts preserved in unconsolidated tephra at El Laco volcano, Chile. *Geology*, *46*(3), 1–4.

Naranjo, J. A., Henríquez, F., & Nyström, J. O. (2010). Subvolcanic contact metasomatism at El Laco Volcanic Complex, Central Andes. *Andean Geology*, *37*(1), 110–120. https://doi.org/10.4067/S0718-71062010000100005

Naslund, H. R., Henríquez, F., Nyström, J. O., Vivallo, W., & Dobbs, F. M. (2002). MAGMATIC IRON ORES AND ASSOCIATED MINERALISATION : EXAMPLES FROM THE CHILEAN HIGH ANDES AND COASTAL Field Relationships at El Laco. *Porter, TM, Hydrothermal Iron Oxide Copper-Gold & Related Deposits: A Global Perspective*, *2*(January 2002), 207–226.

Newbury, D. E., & Ritchie, N. W. M. (2013). Is scanning electron microscopy/energy dispersive X-ray spectrometry (SEM/EDS) quantitative? *Scanning*. https://doi.org/10.1002/sca.21041

Nyström, J. O., & Henriquez, F. (1994). Magmatic features of iron ores of the Kiruna type in Chile and Sweden; ore textures and magnetite geochemistry. *Economic Geology*, *89*(4), 820–839. https://doi.org/10.2113/gsecongeo.89.4.820

Nyström, J. O., Henríquez, F., Naranjo, J. A., & Nasuland, H. R. (2016). Magnetite spherules in pyroclastic iron ore at El Laco, Chile. *American Mineralogist*, *101*(3), 587–595. https://doi.org/10.2138/am-2016-5505

Ovalle, J. T., La Cruz, N. L., Reich, M., Barra, F., Simon, A. C., Konecke, B. A., et al. (2018). Formation of massive iron deposits linked to explosive volcanic eruptions. *Scientific Reports*, *8*(1), 14855. https://doi.org/10.1038/s41598-018-33206-3

Oxford Instruments. (2018). EBSD Sample Preparation - Polishing. Retrieved January 16, 2019, from http://www.ebsd.com/hints-tips-for-ebsd-data-collection/ebsd-sample-preparation/polishing

Park, C. F. (1961). A magnetite “flow” in Northern Chile. *Economic Geology*. https://doi.org/10.2113/gsecongeo.56.2.431

Parkinson, G. S. (2016). Iron oxide surfaces. *Surface Science Reports*, *71*(1), 272–365. https://doi.org/10.1016/j.surfrep.2016.02.001

Rhodes, A. L., Oreskes, N., Sheets, S., & Skinner, B. J. (1999). Geology and rare earth element geochemistry of magnetic deposits at El Laco, Chile. In *Geology and Ore Deposits of the Central Andes* (Vol. 7, pp. 299–332).

Sidhu, P. S., Gilkes, R. J., & Posner, A. M. (1977). Mechanism of the low temperature oxidation of synthetic magnetites. *Journal of Inorganic and Nuclear Chemistry*, *39*(11), 1953–1958. https://doi.org/https://doi.org/10.1016/0022-1902(77)80523-X

Sillitoe, R., & Burrows, D. (2002). Scientific Communications: NEW FIELD EVIDENCE BEARING ON THE ORIGIN OF THE EL LACO MAGNETITE DEPOSIT, NORTHERN CHILE. *Economic Geology*, *97*(2002), 1101–1109. Retrieved from http://www.medicaljournals.se/jrm/content/download.php?doi=10.1080/165019773137

Taylor, P., & Owen, D. G. (1993). *Oxidation of magnetite in aerated aqueous media*. Chalk River, Ontario, Canada: Atomic Energy of Canada Limited. Retrieved from http://www.iaea.org/inis/collection/NCLCollectionStore/_Public/27/000/27000133.pdf

Thomas Novoa, A. (1970). Cuadrángulos Iquique y Caleta Molle : Provincia de Tarapacá : escala 1:50.000, *21*(22), 1–52.

Tornos, F., Velasco, F., Morata, D., Barra, F., & Rojo, M. (2011). Let’s talk ore deposits :

proceedings of the Eleventh Biennial SGA Meeting, Antofagasta, Chile, 26-29 September 2011. Antofagasta, Chile: Ediciones Universidad Católica del Norte (Antofagasta, Chile).

Tornos, F., Velasco, F., & Hanchar, J. M. (2016). Iron-rich melts, magmatic magnetite, and superheated hydrothermal systems: The El Laco deposit, Chile. *Geology*, *44*(6), 427–430. https://doi.org/10.1130/G37705.1

Tornos, F., Velasco, F., & Hanchar, J. M. (2017). The magmatic to magmatic-hydrothermal evolution of the El Laco Deposit (Chile) and its implications for the genesis of magnetite-apatite deposits. *Economic Geology*, *112*(7), 1595–1628. https://doi.org/10.5382/econgeo.2017.4523

Travisany, V., Henriquez, F., & Nystroem, J. O. (1995). Magnetite lava flows in the Pleito-Melon District of the Chilean iron belt. *Economic Geology*, *90*(2), 438–444. https://doi.org/10.2113/gsecongeo.90.2.438

Velasco, F., & Tornos, F. (2012). Insights on the effects of the hydrothermal alteration in the El Laco magnetite deposit (Chile). *Macla*, *16*(2), 210–211.

Young, G. M. (1977). Stratigraphic correlation of upper Proterozoic rocks of northwestern Canada. *Canadian Journal of Earth Sciences*, *14*(8), 1771–1787. https://doi.org/10.1139/e77-151

Appendix

Mineral Identification using EMPA and EDS Analysis

Mineral phases were identified primarily using hand sample and optical observations/methods and EDS. For phases with less certainty and for general purpose confirmation, EMPA work was conducted. More points and phases such as Monazite-(Ce) and Xenotime were measured but are not presented here due to their poorer result quality (uneven cracked surfaces, or grains were simply too small to analyse).

EMPA Point Analysis Results

Table 6: EMPA point analysis for silicates and oxides

Description	BBV wp.	Na2O	K2O	FeO	MgO	CaO	SO3	MnO	Al2O3	TiO2	P2O5	SiO2	Total
82-KFeld-2	7		15.11	0.34		0.02	0.15	0.02	18.24	0.01	0.55	65.24	99.68
82-Jarosite-1	6		9.20	35.51			32.32		4.78	0.60	0.30	0.13	82.84
82-Jarosite-1-2	~6		9.40	35.12		0.01	32.49	0.01	3.95	0.48	0.22	0.10	81.79
82-Jarosite-1-3	8		9.10	34.31			32.55	0.02	4.91	0.59	0.27	0.09	81.85
82-Quartz1	3		0.09	0.88		0.01	0.09		0.13	0.03	0.00	102.26	103.52
82-Quartz1	~3		0.06	0.75		0.01	0.09	0.01	0.15	0.03	0.01	104.17	105.30
BM2-magnetiteN	3			76.25	0.13	0.07			0.23	0.05	0.97	9.58	87.31
BM2-magnetiteN-2	~3			78.19	0.11	0.10		0.00	0.23	0.07		8.02	86.72
BM2-quartzN	4			1.08	0.22	0.05			0.25		0.05	78.84	80.53
BM2-quartzN2	~4	0.12	0.07	0.92	0.21	0.02		0.01	0.17		0.03	95.56	97.11
BM1-smectite1	15	0.01	0.08	4.57	0.18	0.74			29.21		0.33	53.22	88.33
BM1-smectite2	16		0.26	15.14	0.72	1.75		0.03	16.18		1.54	53.13	88.76
BM1-smectite3	17		0.29	17.14	0.74	1.83		0.02	16.59		4.49	46.90	88.01
BM1-smectite4	18		0.23	12.89	0.43	1.72		0.02	17.97		1.20	49.25	83.70
Evan garnet	n/a	0.00		22.65	10.82	4.15			22.16		0.05	40.36	100.18

Table 7: EMPA point analysis for phosphates

Description	BBV wp.	F	P2O5	CaO	FeO	Na2O	SO3	Cl	SiO2	Total	O≡F,Cl	Total
BM2-FePO-1	2	0.24	29.23	0.29	45.03		0.23	0.03	2.64	77.69		
BM2-FePO-2	~2	0.28	30.91	0.27	45.55	1.40	0.18	0.01	0.71	79.31		
BM2-apatite1	1	3.53	39.89	52.22	0.62	0.57	1.27	0.79	2.03	100.91	1.66	99.25
BM2-apatite2	13	3.39	40.54	53.47	1.00	0.60	1.47	0.75	0.23	101.46	1.60	99.86
BM2-apatite3	14	3.50	41.49	54.92	0.05	0.46	0.79	0.67	0.15	102.03	1.62	100.40
BM2-apatite4	15	3.29	41.36	54.44	0.82	0.41	0.77	0.77	0.16	102.02	1.56	100.46
BM2-apatite5	5	3.15	40.99	54.00	1.40	0.51	0.97	0.64	0.17	101.82	1.47	100.35
BM1-apatite1	13	2.98	40.08	54.20	0.05	0.36	0.85	0.84	0.48	99.83	1.44	98.38
BM1-apatite2	14	2.90	40.72	54.49	0.03	0.37	0.89	0.85	0.46	100.71	1.41	99.30
BM1-FePO-1	9	0.08	33.26	0.09	57.49	0.06	0.77	0.02	0.43	92.19		
BM1-FePO-2	8	0.15	33.51	0.02	56.96	0.04	0.57	0.01	0.21	91.48		
P4-FePO-1	18	0.12	35.59	0.02	56.07		0.35	0.01	0.04	92.18		
P4-FePO-2	20	0.08	35.94	0.04	55.18		0.29		0.04	91.57		
P4-FePO-3	19	0.05	35.26	0.06	55.00		0.41	0.01	0.03	90.81		

Table 8: EMPA point analysis for sulphates

Description	BBV wp.	SrO	CaO	BaO	FeO	SO3	Total
82-anhydrite-1	~5		38.59	0.03	0.43	54.81	93.87
82-anhydrite-2	5		39.01	0.02	0.34	56.76	96.14
BM2-Barite-1	8	1.36	0.16	64.16	0.43	32.95	99.06

EDS Point Analysis Results

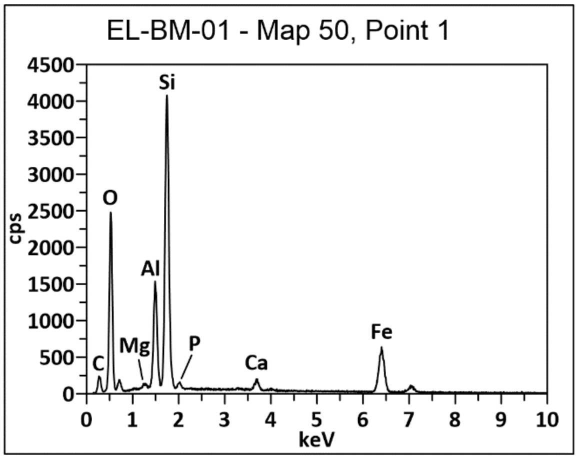

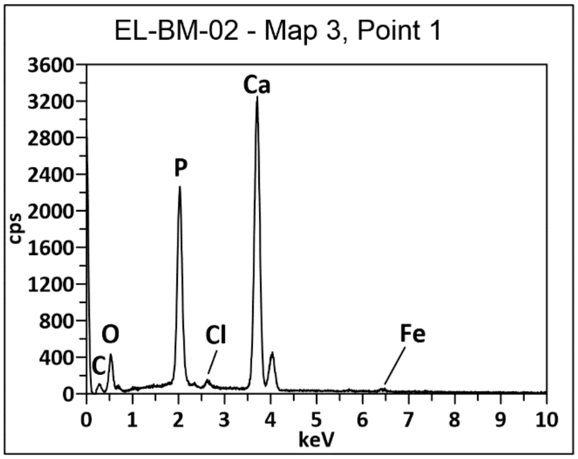

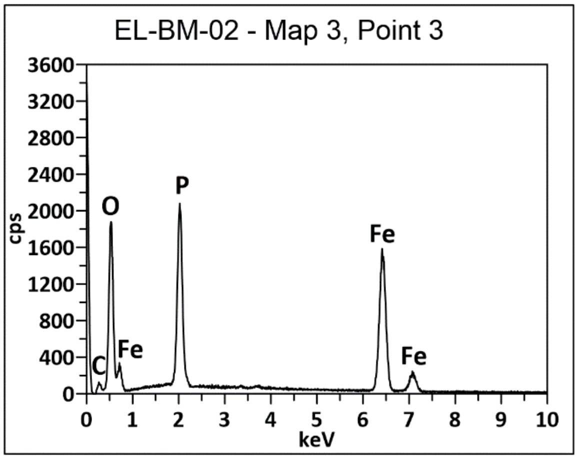

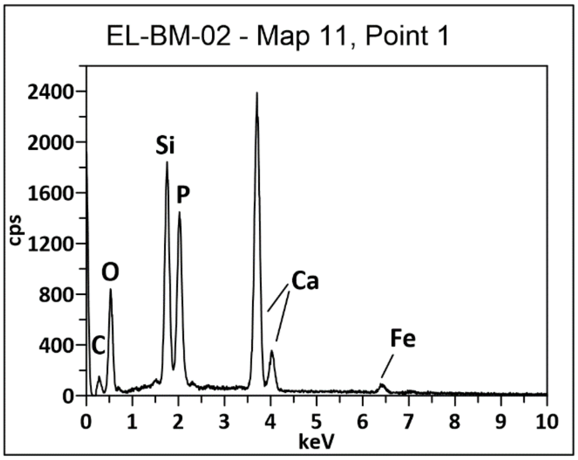

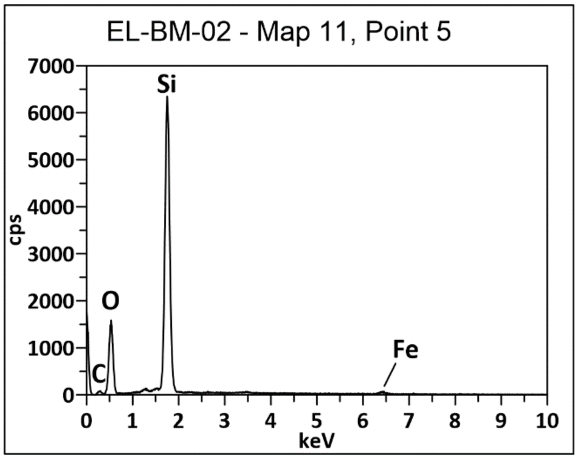

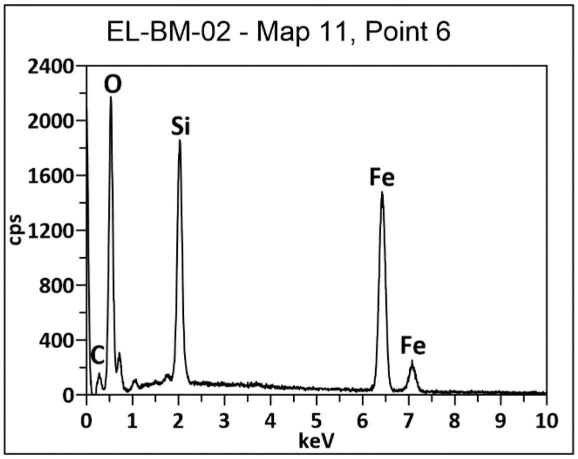

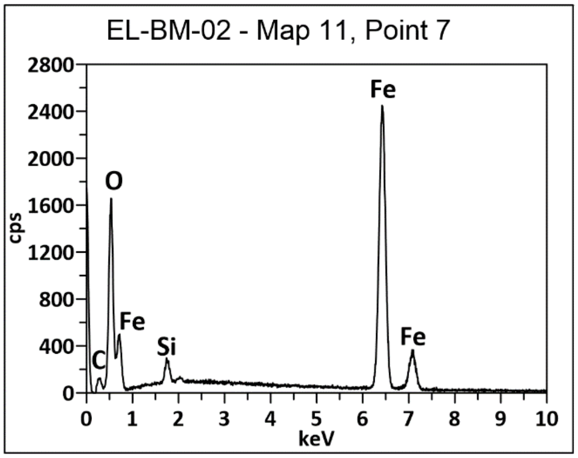
EL-BM-02 - Map 11, Point 7

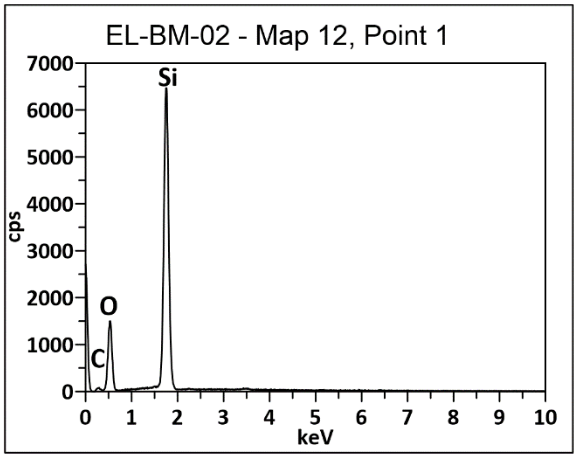
EL-BM-02 - Map 12, Point 1

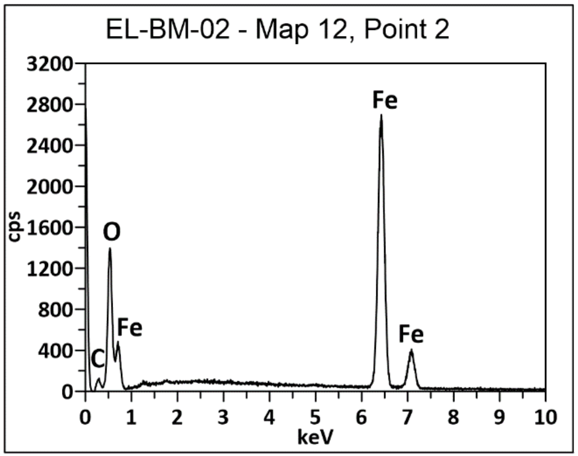
EL-BM-02 - Map 12, Point 2

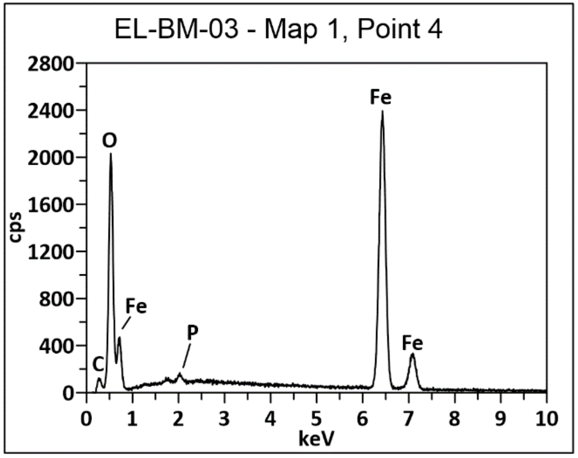
EL-BM-03 - Map 1, Point 4

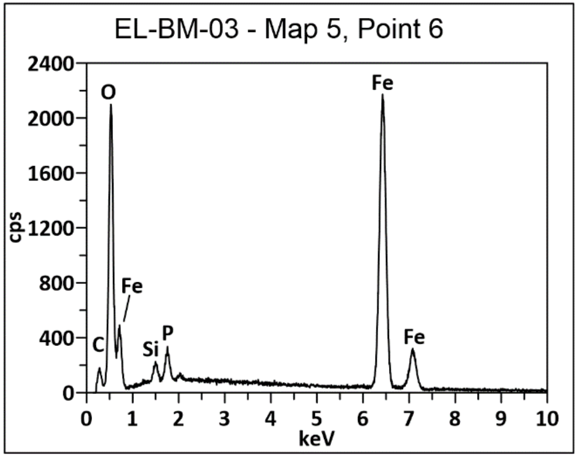
EL-BM-03 - Map 5, Point 6

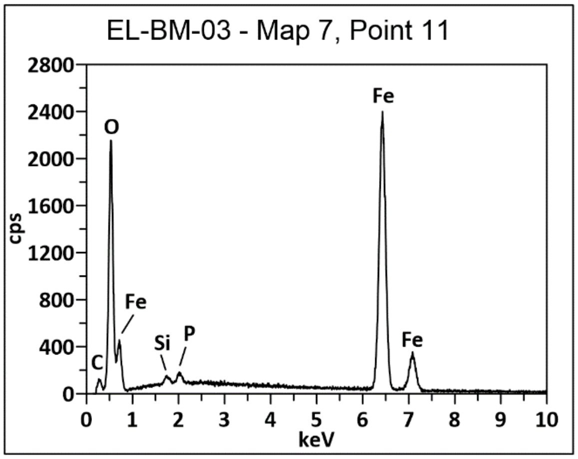
EL-BM-03 - Map 7, Point 11

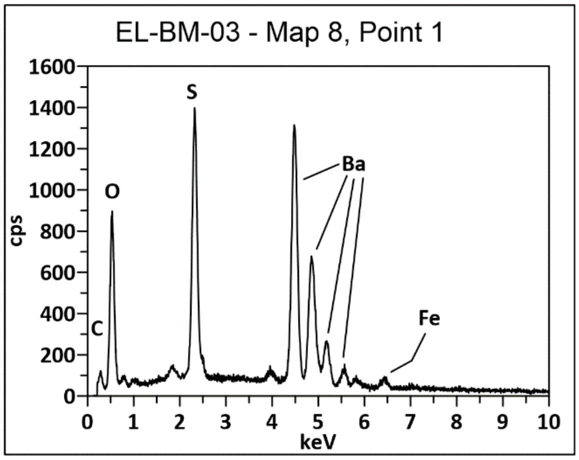
EL-BM-03 - Map 8, Point 1

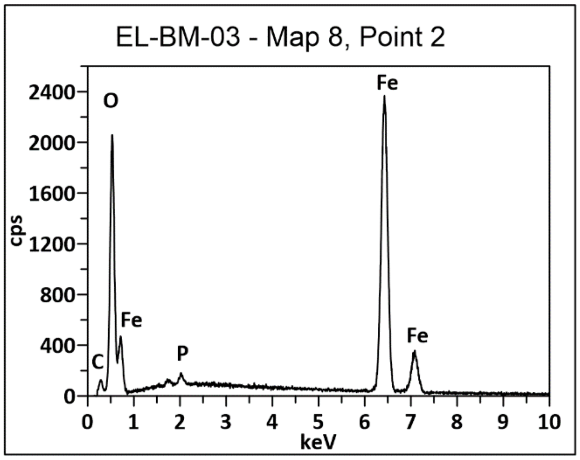
EL-BM-03 - Map 8, Point 2

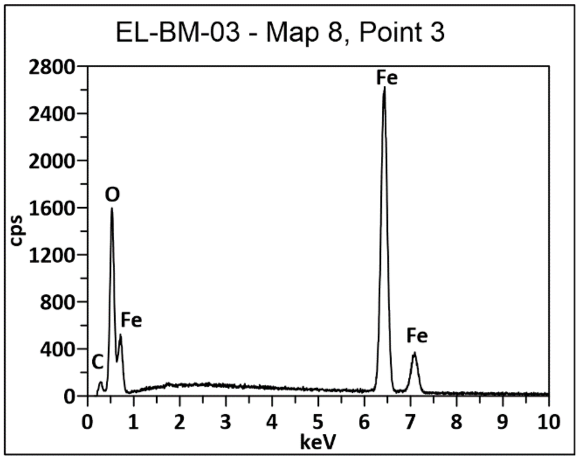
EL-BM-03 - Map 8, Point 3

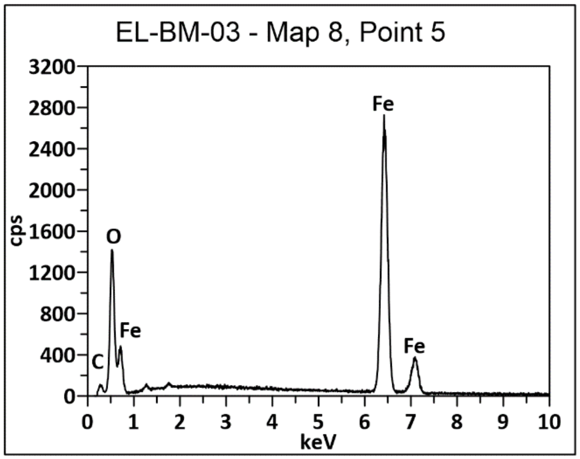
EL-BM-03 - Map 8, Point 5

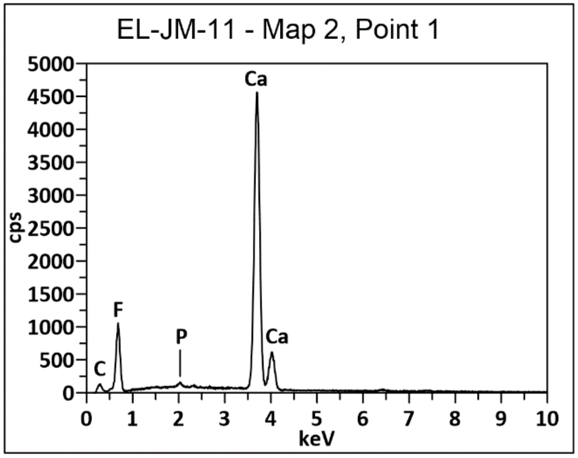
EL-JM-11 - Map 2, Point 1

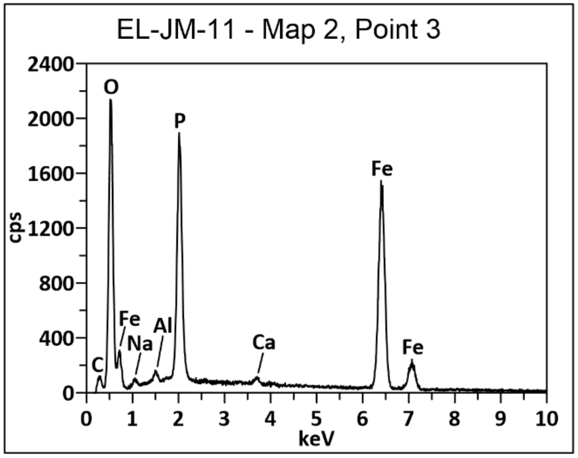
EL-JM-11 - Map 2, Point 3

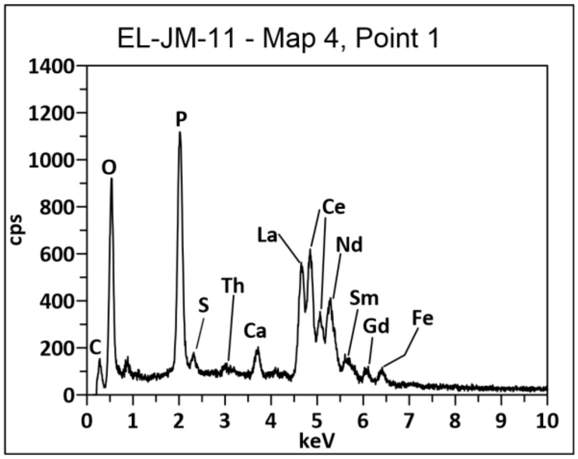
EL-JM-11 - Map 4, Point 1

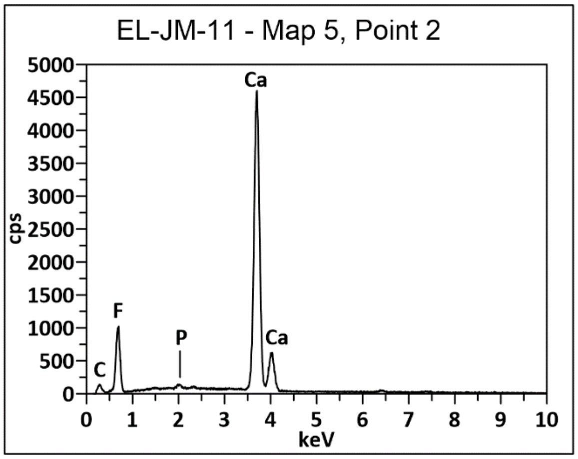
EL-JM-11 - Map 5, Point 2

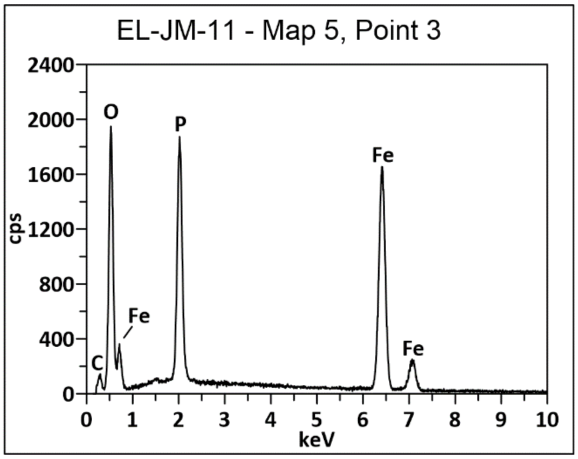
EL-JM-11 - Map 5, Point 3

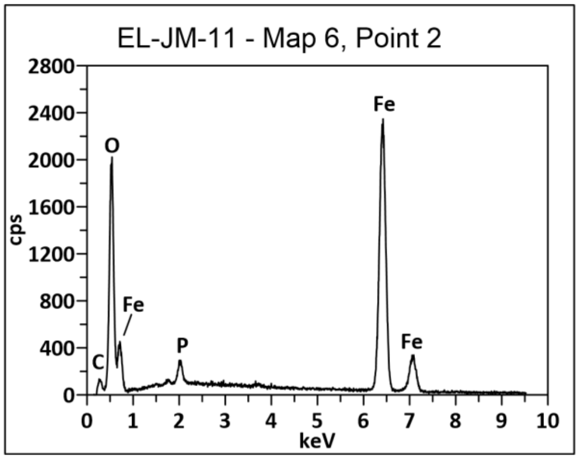
EL-JM-11 - Map 6, Point 2

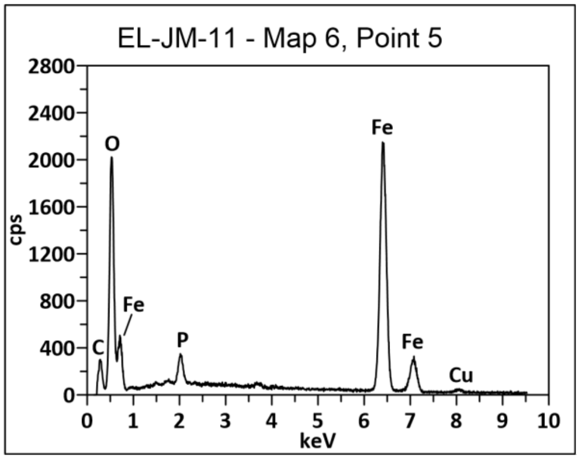
EL-JM-11 - Map 6, Point 5

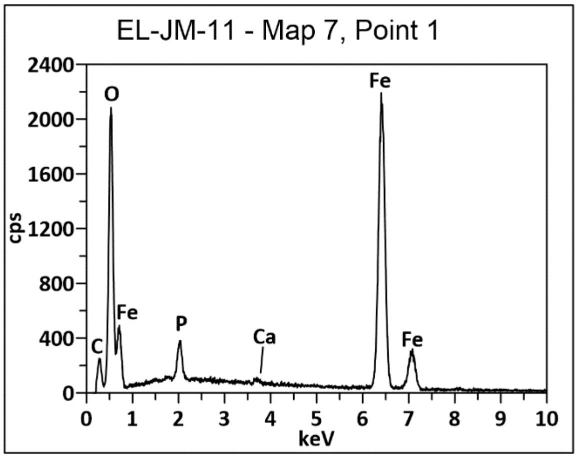
EL-JM-11 - Map 7, Point 1

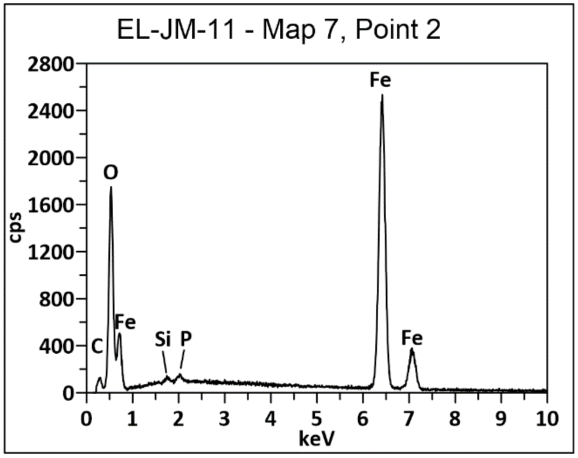
EL-JM-11 - Map 7, Point 2

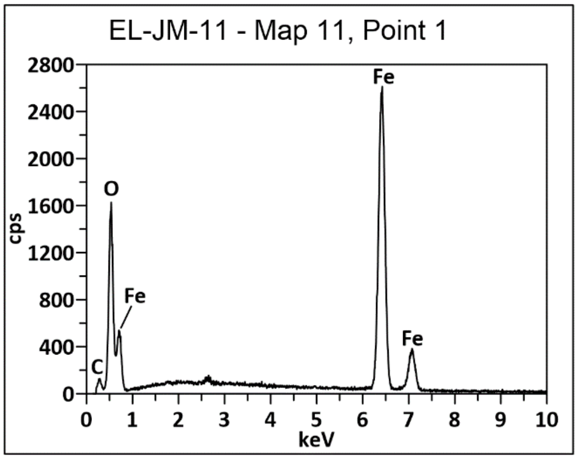
EL-JM-11 - Map 11, Point 1

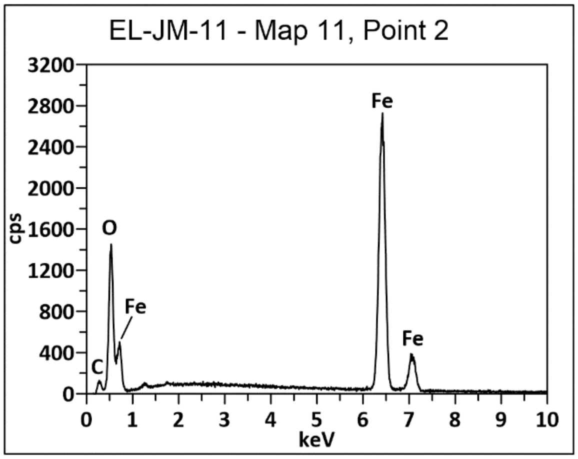
EL-JM-11 - Map 11, Point 2

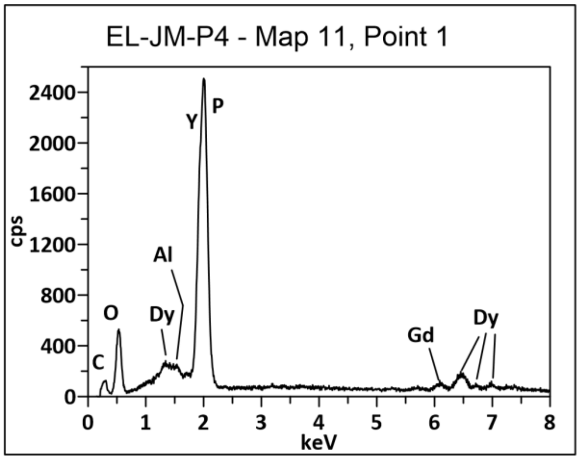
EL-JM-P4 - Map 11, Point 1

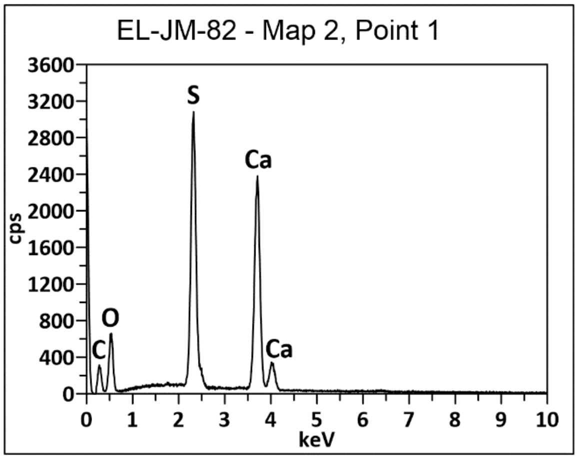
EL-JM-82 - Map 2, Point 1

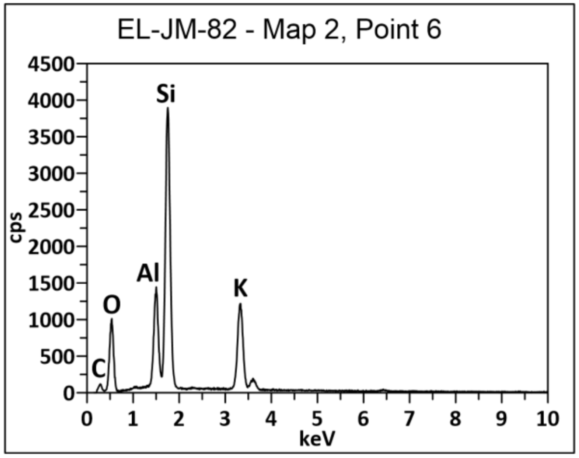
EL-JM-82 - Map 2, Point 6

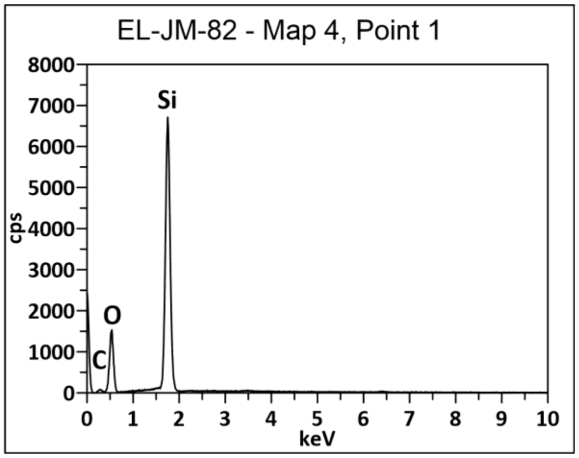
EL-JM-82 - Map 4, Point 1

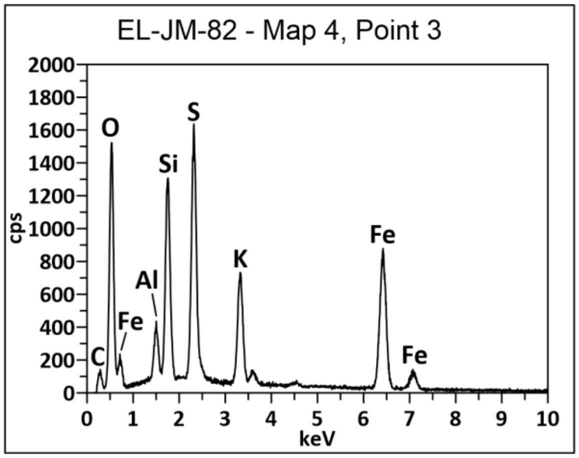
EL-JM-82 - Map 4, Point 3

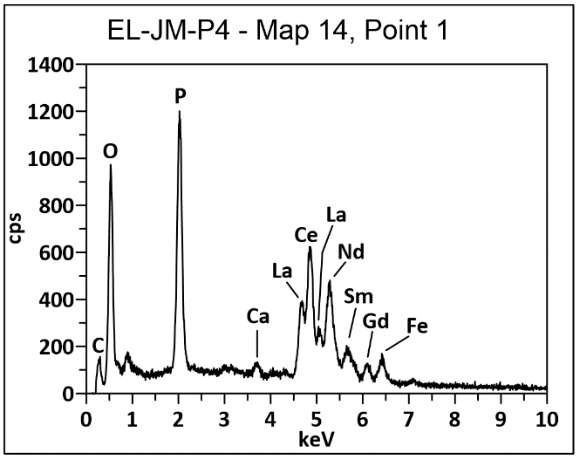
EL-JM-P4 - Map 14, Point 1